
Toward a Thermochemical Model of the Evolution of the Earth's Mantle

Uwe Walzer¹, Roland Hendel¹, and John Baumgardner²

¹ Institut für Geowissenschaften, Friedrich-Schiller-Universität,
Burgweg 11, 07749 Jena, Germany u.walzer@uni-jena.de

² Los Alamos National Laboratory, MS B216 T-3, Los Alamos, NM 87545, USA

Summary. This is a report on first steps for a combination of two numerical models of the evolution of the Earth's mantle: The first one, K3, is a new 2-D convection-fractionation model that simulates the growth of continents and of the geochemically complementary depleted mantle reservoir. The second model shows the 3-D generation of oceanic lithospheric plates and subducting sheet-like downwellings in a spherical-shell mantle. Based on the abundances of the present-day geochemical reservoirs of Hofmann (1988) we developed a numerical dynamical model of convection and of chemical differentiation in the Earth's mantle. It is shown that a growing and additionally laterally moving continent and a growing depleted mantle evolved from an initially homogeneous primordial mantle. The internal heat production density of the evolving mantle depends on the redistribution of the radioactive elements by fractionation and convection. The fractionation generates separate geochemical reservoirs. However, the convection blurs the reservoirs by mixing. Although we take into account also the effects of the two phase transitions in 410 and 660 km depth, it is essentially the dependence of the viscosity on radius which guarantees the conservation of the major geochemical reservoirs. This model has no internal compulsory conditions. The principal idea of this first model is to compute the relative viscosity variations as a function of depth from observable quantities. We develop a self-consistent theory using the Helmholtz free energy, the Ullmann-Pan'kov equation of state, the free volume Grüneisen parameter and Gilvarry's formulation of Lindemann's law. In order to receive the relative variations of the radial factor of the viscosity, we insert the pressure, P , the bulk modulus, K , and $\partial K/\partial P$ from PREM. For mantle layers deeper than 771 km we used the perovskite melting curve by Zerr and Boehler (1993, 1994) in order to estimate the relative viscosity. For the calibration of the viscosity we have chosen the standard postglacial-uplift viscosity beneath the continental lithosphere. Furthermore, we took into account the dependence of the viscosity on temperature and on the degree of depletion of volatiles. An essential first new result of this paper is a *high-viscosity transition layer* and a *second low-viscosity layer* below it. Although our model mantle is essentially heated from within, we assume additionally a small heat flow at the CMB. This is necessary because of the dynamo theory of the outer core. The second main result of this first model is a *more distinct bipartition of the mantle* in a depleted upper part and a lower part rich in incompatible elements, yet. This result is rather insensit-

ive to variations of the Rayleigh number and of the thermal boundary condition at CMB. The different parts of this paper are closely connected by the algorithm. The continuation of the first finding leads to a 3-D, up to now purely thermal model of mantle evolution and plate generation. This second model was used to carry out a series of three-dimensional compressible spherical-shell convection calculations with another new, but related viscosity profile, called *eta3*, that is derived from PREM and mineral physics, only. Here, the Birch-Murnaghan equation was used to derive the Grüneisen parameter as a function of depth. Adding the pressure dependence of the thermal expansion coefficient of mantle minerals, we derived the specific heats, c_p and c_v , too. Using the Gilvarry formulation, we found a new melting temperature of the mantle and the new viscosity profile, *eta3*. The features of *eta3* are a high-viscosity transition layer, a second low-viscosity layer beginning under the 660-km discontinuity, and a strong viscosity maximum in the central parts of the lower mantle. The rheology is Newtonian but it is supplemented by a viscoplastic yield stress, σ_y . A viscosity-level parameter, r_n , and σ_y have been varied. For a medium-sized Rayleigh-number-yield-stress area, *eta3* generates a stable, plate-tectonic behavior near the surface and simultaneously thin sheet-like downwellings in the depth. Outside this area three other types of solution were found. The presence of *two* internal low-viscosity layers and of σ_y is obviously conducive for flatness and thin sheet-like downwellings. The distribution of the downwellings is more Earth-like if the yield stress is added. The outlines of a combination of the two models have been discussed.

1 Introduction

1.1 Two essential problems

Two essential problems occur in the event of modelling the evolution of the Earth's mantle:

- a) Oceanic plateaus develop by chemical differentiation leaving behind the depleted mantle that does not occupy the whole mantle. It is well-known that other mantle reservoirs exist which are rich in incompatible elements, yet. On the other hand, seismic tomography and geodynamic modelling show that whole-mantle convection exists at least at the present time. Using viscosity distributions with small contrasts, whole-mantle convection would destroy the extensive geochemical mantle reservoirs: The mantle would be homogenized by stirring. The enriched oceanic plateau basalts are carried by the conveying belt, the normal oceanic lithosphere, to the continent that grows by accretion of terranes. So, we have to model the growth of the total continental mass, and the model must explain the conservation of the mantle reservoirs in spite of whole-mantle convection.
- b) Oceanic lithospheric plates arise by ocean spreading on one side. They push forward or subduct on the other side. In between, the oceanic lithospheric plates rotate like a thin solid spherical shell around the center of the Earth. In this way, the terrestrial lithosphere is piecewise rotating with different directions of the angular velocity vector for the different plates. Such

a behavior cannot be produced by purely viscous mantle models. In addition to this, viscous models with small viscosity contrasts show rather thick downwellings but not *very thin* sheet-like downwellings.

We developed two models to solve the two mentioned problems. The models have the following features in common: From solid-state physics and the seismic model PREM, we deduce new mantle-viscosity profiles that show not only a highly viscous oceanic lithosphere as the upper thermal boundary layer and a low-viscosity asthenosphere below of it but also the following new features: The transition layer is highly viscous with steep viscosity gradients at its boundaries. A second low-viscosity layer lays under the 660-km discontinuity followed by a thick high-viscosity layer in the deep or the central parts of the lower mantle, respectively. This last mentioned layer has gentle viscosity slopes. Finally, a viscosity decrease is observed above the CMB. The latter thermal boundary layer is well-known from other models.

Developing a new 2-D convection-fractionation model, K3, the evolution of the continent and the complementary depleted mantle reservoir was calculated. The highly viscous deeper layer of the lower mantle and the partial screening by the high-viscosity transition layer cause the conservation of a deeper reservoir with high U, Th and K abundances. On the other hand, the faster convective creeping in the low-viscosity asthenosphere generates a strong homogenization of the MORB source. Growth and lateral movement of the model continent have Earth-like rates. The evolution of the laterally averaged surface heat flow of the models proves to be at realistic magnitudes. Plumes form a reference frame for the lateral movement of the continent in the models K3A and K3B (cf. sections 2 and 3) and for the lateral movement of the oceanic lithospheric plate of model S2 (cf. Sections 4 and 5) since the maintenance of a low-viscosity tube through the thick high-viscous layer of the lower mantle needs less energy than the production of a new tube or the lateral movement of the tube.

Our 3-D spherical-shell model (model S2) shows that the existence of two low-viscosity layers inside the mantle causes very thin tabular-shaped downwellings. This applies also for purely Newtonian-fluid models. But only the supplementation by a viscoplastic yield stress, σ_y , leads to a stable, plate-tectonic behavior *near the surface*. For infinite yield stress, the cold sheet-like downwellings are reticularly connected. For moderate, rock-like yield stress values, the sheet-like downwellings show a more Earth-like distribution.

There are different proposals to explain the conservation of geochemical mantle reservoirs in spite of whole-mantle convection. Walzer and Hendel (1997 a, b, 1999) computed a 2-D dynamical model of thermal convection including the mentioned chemical differentiation using active tracers. A highly viscous lower part of the lower mantle makes it possible to conserve enriched reservoirs. This model did not include a high-viscosity transition layer. The differences between the major geochemical reservoirs are confined to U, Th and K in that model whereas the major-element composition (SiO_2 , MgO, FeO, Al_2O_3 , CaO) of the mantle is supposed to be homogeneous for simplic-

ity and in accordance with O'Neill and Palme (1998). However, Kellogg et al. (1999) proposed a model with a global geochemical boundary in the interior of the lower mantle. This hypothetical chemical jump includes also the major-element composition and a 1%-density discontinuity. This assumption contradicts tomographic results according to Tackley (2002). Bercovici and Karato (2003) explain the distinct chemical signatures between mid-ocean ridge and ocean-island basalts by a water-filter hypothesis. The subduction of the down-going slabs produces an ascending ambient mantle. They consider the transition zone to be a high-water-solubility zone. As the ambient mantle rises out of the transition layer into the low-solubility asthenosphere, it undergoes dehydration by partial melting that filters out U, T, K and other incompatible elements. The water-rich, enriched residue returns to the transition zone or deeper whereas the depleted rock becomes the asthenospheric depleted reservoir. Xie and Tackley (2003) made another interesting suggestion. They proposed an outgassing model taking into account the partition coefficients of helium and argon. The results indicate that the system self-consistently evolves regions with the measured range of $^3\text{He}/^4\text{He}$. For some special parameter combinations, Xie and Tackley (2003) arrive at proper $^3\text{He}/^4\text{He}$ ratios of volcanic rocks and at about 50% outgassing of ^{40}Ar . To this encouraging results we want to add a further proposal that is suitable as a solution of the paradox of the simultaneous existence of durable mantle reservoirs and whole-mantle convection.

1.2 General reflections on the 2-D convection-fractionation model K3

In the first part this paper we present a model of the evolution of the Earth's mantle starting from some geochemical findings. For the proper computations, however, only some numerical results of Hofmann (1988, 1997) are important. So, for the acceptance of our model only parts of our geochemical discussion are really necessary, however, the other parts are relevant to understand the background. The assumptions of the model are some thermodynamic deductions, some results of solid-state physics and a well-known radial distribution of seismological quantities. The evolution model is not based on parameterized basic equations but on the full set of balance equations which have been solved dynamically and numerically. The formation of the oceanic plateaus out of partial melt volumes in the uppermost part of the mantle is included in the model in a simplified way by a tracer approach. The model continent emerges by the accretion of oceanic plateaus. The model-continent's growth function and lateral continental-drift velocity, both as a function of time, have been computed and compared with observational data. The physics of the more relevant phase boundaries at 410 and 660 km depth is included. However, in accordance with Bunge et al. (1997) we concluded by numerical experience that the spatial and temporal distribution of the viscosity has a greater influence on the solid-state flow field than the phase transitions. Therefore we

investigated the viscosity problem deeper than in our earlier investigations. The present model differs from our preceding model (Walzer and Hendel, 1999) by new physical derivations and by a new approach to the viscosity problem. The influences of some individual assumptions of the model have been tested individually in order to check the numerical correctness and to understand the individual features of the physical mechanism. It is evident that by our present 2-D system, called K3A, a lot of resulting quantities are inseparably linked with one another. Their essential features should correspond with observations: the spatial and temporal distribution of creeping velocity, the present-day heat flows of continents and oceans at the surface, the laterally averaged temperature and the laterally averaged viscosity as a function of depth and, last not least, the existence of a depleted mantle with a rather homogenized distribution of incompatible elements beneath the lithosphere. There are chemical reservoirs in the mantle in spite of the convective mixing which is operating since at least 4.49×10^9 a and which is continuously working against the formation of the chemical reservoirs. The essence of this paper is the integration of the mentioned fields of work.

1.3 Geochemical considerations

Because of studies of the oxygen-isotope distribution it is unlikely that the building blocks of the Earth originated from a mixture of the three major groups of chondrites, namely carbonaceous, enstatite and ordinary chondrites (Clayton and Mayeda, 1996). Obviously, a multitude of chemical differentiation processes operated in the protosolar cloud and the present-day meteorites are the remaining stock which has not been exhausted for the formation of planets. From the chemical point of view, the Earth accreted in a rather complex way (O'Neill and Palme, 1998). We maintain the conception that the continent develops by chemical differentiation (via two steps) from parts of the mantle which are rich in incompatible elements (see e. g. McCulloch and Bennett, 1998). This assumption leads to strictly chondritic ratios of the refractory lithophile elements (RLE). For that and other reasons, a lot of similarities to chondrites are maintained, in spite of the opening remark of this Section. O'Neill and Palme (1998) have concluded on the base of the chondritic ratios of the RLE in the upper mantle, from the secular evolution of ε_{Nd} and ε_{Hf} and their present values and from the near-chondritic Re/Os mass ratio in the upper mantle that there is no gross compositional layering in the mantle. In other words: The mass percentage of the most abundant chemical elements is homogeneously distributed in the mantle without the D" layer. If we write below on a depleted mantle (DM) and a pristine mantle (PM) then we refer to the different abundances in incompatible elements where U, Th and K are relevant for the internal heating of the mantle. So, we do not refer to a gross chemical layering. The most meteorites, which have been found, came into being between 4.56 Ga and 4.54 Ga ago (Dalrymple, 1991). The chemically related material, from which the Earth developed via some stages

(Wetherill, 1986), should have had similar ages. So the accretion of the Earth cannot have been earlier than 4.56 Ga. If about 0.07×10^9 a are necessary for the segregation into metallic core and silicate mantle than (or from the U/Pb fractionation of the Earth) it follows that the formation of the Earth's core and primordial mantle was finished before $(4.49 \pm 0.03) \times 10^9$ a (McCulloch and Bennett, 1998). Therefore in our present model, K3, the evolution of the homogeneous primordial mantle begins at an age of 4.49×10^9 a. We assume that since that time the silicate mantle was virtually chemically isolated from the metallic core because there is no perceivable change in siderophile element concentration of mantle-derived rocks in the last 4.0×10^9 a for which terrestrial rocks have been found (O'Neill and Palme, 1998). McCulloch and Bennett (1998) concluded chemical isolation of the core from the terrestrial evolution of the Pb and Os isotopes. Therefore in our model there is only a thermal connection between core and mantle by emitting $20 \text{ mW} \cdot \text{m}^{-2}$ from the core. The full justification is in Stacey's (1992) Section 6.7.5 entitled Constancy of the Core-to-Mantle Heat Flux and Appendix A of Walzer and Hendel (1999). [In our 3-D spherical-shell model (Walzer et al., 2004), we abandoned, however, this thermal CMB boundary condition taking into account the dynamical core cooling and the *laterally* constant CMB temperature.] It is well known that there are different views on the recycling of continental crust. Armstrong (1968, 1991) advocated the opinion that a continental crust of present-day size developed prior to 4 Ga and that this mass has been reduced through subduction of continent-derived sediments and that on the other hand continental mass has been added by the accretion of island arcs. So the amount of the continental mass near the surface would be approximately constant. In a few ocean-island basalts, small amounts (less than 2 %) have been found which possibly stem from continentally derived sediments (Woodhead and McCulloch, 1989). The other opinion is that the continental-crust mass has grown through time and that the subduction of continental crust is neglectable (Taylor and McLennan, 1985). If a continental-crust mass with a present-day amount existed before 4.0 Ga, the big amounts of sediments, e.g. also detrital zircons, should be detectable in the Archean sediments after that. However, in spite of intensive investigations using U-Pb and Lu-Hf measurements of the mentioned early Archean sedimentary zircons, no big mass amounts before 4.0 Ga have been found (Nutman et al., 1996; McCulloch and Bennett, 1998). Hofmann (1997) emphasized that not only the geochemical conclusions from Pb isotopes, but also the Nb/U and Ce/Pb ratios rule out large amounts of recycled continental-crust material in ocean-island basalts (OIB) except in cases of EM-2 OIB and Indian Ocean MORB. On the other hand, plateaus of oceanic flood basalts with enhanced concentrations of incompatible elements have a Moho deeper than normal MORB oceanic crust. They will be attached to the continent. For the mentioned reasons we assumed in this model a growing continental crust scenario without subduction of continental material. However, subduction of oceanic lithosphere is included. We do not introduce any assumption on the sequence of accretion events of the oceanic plateaus to the

continent, but it is a *result* of the dynamics of our model system. We *obtain* episodic continental growth phases and no continuous growth. These results correspond with the observation that the real continents grow episodically (McCulloch and Bennett, 1994; Condie, 1998; Yale and Carpenter, 1998).

2 Theory of model K3

2.1 Model of K and K'

For a mantle without gross compositional layering or for a single mineral, and for a rather general class of equations of state (EoS), the equation

$$\frac{dK}{dP} = K'_0 + \frac{1}{9}(1 + K'_0)(1 - 2K'_0)\frac{P}{K} \quad (2.1)$$

can be derived where P is the pressure, K the isothermal bulk modulus and K'_0 the pressure derivative of the bulk modulus at vanishing pressure. The formula has been proved by Ullmann and Pankov (1976). Using additionally thermodynamics, plus results by Anderson (1995) and Poirier (1991), this relation can be found in a shorter way. We use the relation

$$U = \frac{9}{2} \frac{K_0}{(2 - K'_0)^2} \left[x^{(2-K'_0)/3} - 1 \right]^2 \quad (2.2)$$

as an ansatz for the Helmholtz free energy density. For a deduction of (2.1) and (2.2), see Appendix C. From the negative derivative of U according to x we receive the Ullmann-Pan'kov equation of state (EoS)

$$P = \frac{3K_0}{(K'_0 - 2)} \left[x^{(1-2K'_0)/3} - x^{-(1+K'_0)/3} \right] \quad (2.3)$$

where x is the the ratio of the density at zero pressure to the density. The amounts of the K'_0 of a lot of rocks and minerals are near 4. Inserting $K'_0 = 4$ in eq (2.3) we get the second-order Birch-Murnaghan EoS:

$$P = \frac{3K_0}{2} \left[x^{-7/3} - x^{-5/3} \right] \quad (2.4)$$

Therefore, this equation is a special case of the Ullmann-Pan'kov EoS. Ullmann and Pan'kov (1976) have shown by comparison with experimental high pressure data that eq (2.3) is better than the Birch-Murnaghan equation if K'_0 is not in the surrounding of $K'_0 = 4$. Near $K'_0 = 4$, of course, both EoS have the same quality. Moreover, Walzer et al. (1979) proved by a comparison with experimental high-compression data that eq (2.3) is superior to the Thomsen EoS (Thomsen, 1970) and to the fourth-order anharmonic theory by Leibfried and Ludwig (1961). Anderson (1995) demonstrated that the values of $K_0K''_0$ for the Birch-Murnaghan EoS and for the Ullmann-Pan'kov EoS

deviate only slightly from each other for vanishing remainder terms, $Y_4 = 0$, and for $K'_0 = 3.5, 5.0$ and 6.5 , accordingly in the practically relevant range of K'_0 . The $K_0 K''_0$ deviations from the values of our two favourite equations of state are greater for the Bardeen EoS and decidedly strong for the Thomsen EoS. These results are fully coincident with the experiences of our group. Therefore, we recommend the Ullmann-Pan'kov EoS *for silicates and oxides*. The Birch-Murnaghan EoS does as well in the most investigations. However, for minerals with relatively high K'_0 the experimental values of the density and the bulk modulus as a function of pressure are better approximated by (2.3) and (2.6), respectively. The isothermal bulk modulus is defined by

$$K = -x(\partial P/\partial x)_T \quad (2.5)$$

The isothermal bulk modulus for silicates and oxides has been computed combining eqs (2.3) and (2.5):

$$K = \frac{K_0}{(K'_0 - 2)} \left[(2K'_0 - 1)x^{(1-2K'_0)/3} - (K'_0 + 1)x^{-(1+K'_0)/3} \right] \quad (2.6)$$

2.2 The melting temperature of model K3

First of all we search for a relation between the melting temperature, T_m , and the volume ratio, x , because the activation enthalpy can be replaced by a product of a constant by the melting temperature in the dependence of the shear viscosity on pressure and temperature. For close-packed materials, Stacey and Irvine (1977a, b) found that Gilvarry's (1956) formulation of Lindemann's melting law can be written as follows:

$$\frac{d \ln T_m}{dP} = \frac{2(\gamma - 1/3)}{K} \quad (2.7)$$

In this formula, not only the bulk modulus, K , but also the Grüneisen ratio, γ , depends on x . From eqs (2.5) and (2.7), it follows that

$$\frac{d \ln T_m}{d \ln x} = 2 \left(\frac{1}{3} - \gamma \right) \quad (2.8)$$

Restricted to halides, already Vashchenko and Zubarev (1963) arrived at the free volume gamma. However, Irvine and Stacey (1975) calculated the free-volume gamma taking into consideration the coupled three-dimensional vibrations in a fcc crystal. Indirectly, also the high-frequency modes have been taken into account. The result is:

$$\gamma_{vz} = \left[\frac{1}{2} \frac{dK}{dP} - \frac{5}{6} + \frac{2}{9} \frac{P}{K} \right] / \left[1 - \frac{4}{3} \frac{P}{K} \right] \quad (2.9)$$

It is possible to prove that eq (2.9) applies also for other forms of closest packing. Using eqs (2.1), (2.3), (2.6) and (2.9) we receive the dependence of the Grüneisen parameter on x :

$$\gamma = \frac{K'_0 - 1}{3} + \frac{1}{6} \frac{(K'_0 - 2)(K'_0 - 3)}{(2K'_0 - 5)x^{(2-K'_0)/3} - K'_0 + 3} \quad (2.10)$$

Inserting this relation in eq (2.8) we get a differential equation. We could solve it analytically. This solution is

$$T_m = T_{mo\lambda} \cdot f_2(x) \quad (2.11)$$

where the index λ denotes mineralogically different mantle shells and the function f_2 is defined as follows.

$$f_2 = \exp \left\{ \frac{1}{3}(2 - K'_0) \ln x + \ln \left[(2K'_0 - 5) \cdot \exp \left(\frac{1}{3}(2 - K'_0) \ln x \right) - K'_0 + 3 \right] \right\} \quad (2.12)$$

Even for a single mineral, it is often a difficult job to determine K'_0 experimentally. It is more difficult for a rock, especially if the mixture of minerals is only approximately known. Therefore we try to estimate the mantle's K'_0 from *observable* quantities. Dziewonski and Anderson (1981) derived a self-consistent Earth model, called PREM, where the needed quantities are given as functions of the radius in Table II. The mentioned quantities are the pressure P , the bulk modulus K and $\partial K/\partial P$, where K is called kappa in PREM. Inserting these quantities in eq (2.1) we receive K'_0 as a function of depth. In that large regions of the mantle where the depth is a monotonous function of x , we insert the K'_0 values in eq (2.12). So we receive the relative variations of the melting temperature as a function of depth. We took $x = \rho_{o\lambda}/\rho$, where ρ is the density from PREM. The density ρ is assigned to a depth in Table II of PREM, $\rho_{o\lambda}$ is the zero-pressure density of the most important mineral of the mantle shell with index λ . If it is feasible to estimate $T_{mo\lambda}$ for each shell of the mantle then we get T_m as function of depth.

2.3 The viscosity of model K3

We compute the viscosity by means of

$$\eta = \eta_{o\lambda} \cdot \exp \left[\frac{k_{2\lambda} \cdot f_2(x_3) \cdot T_{mo\lambda}}{T(x_1, x_3, t)} \right] \cdot \left(\frac{A_{dry}}{A_{wet}} \right)^{0.5D'} \cdot \exp \left[\frac{0.5 \cdot D' \cdot \Delta E_c^*}{R \cdot T(x_1, x_3, t)} \right] \quad (2.13)$$

where T is the dimensional absolute temperature in degrees Kelvin, x_1 , x_2 and x_3 denote the Cartesian components of the location vector, x_3 is the vertical component, where the origin is at the core-mantle boundary. t signifies the time. The *last* two factors of the right-hand side of eq (2.13) are explained in Doin et al. (1997). They are relevant only in the continent. These factors reflect the stiffer depleted continental lithosphere. One of the differences between the mentioned paper and our paper is that our continent is not simply put on the remaining mantle but the continent evolves via an intermediate product, the oceanic plateaus, by the dynamics of the chemical segregation in

the asthenosphere episodically from mantle material. The episodic character is not an assumption but a computational result. The growth of the model continent is caused by the addition of oceanic plateaus to the fertile continental margin. D' is the degree of depletion of volatiles. According to Doin et al. (1997) we take into account the case where the difference in water content between the depleted continental lithosphere and the mantle is one half of the water content of a water-saturated peridotite. The ratio of the preexponential constants in the Arrhenius law is taken to be $A_{dry}/A_{wet} = 7.9 \times 10^{-3}$. The difference of the activation energies is $\Delta E_c^* = E_{dry}^* - E_{wet}^* = 10^5 Jmol^{-1}$ (Karato and Wu, 1993). R is the gas constant. It is evident that we can assume $D' = 0$ for the greater part of the mantle. In this case the two right factors of the right-hand side of eq (2.13) are unity. The influence of the last two factors of the right-hand side of the eq (2.13) on the overall mechanism is low. Essentially, the two factors cause that the continental heat flow is lower than the averaged oceanic heat flow. Physical investigations by Karato and Li (1992) and Li et al. (1996) have shown that the viscosity of the lower mantle is controlled by diffusion creep. The same applies for the deep upper mantle (Karato and Wu, 1993). It is still unclear what rheology is appropriate for the asthenosphere (beneath the lithosphere). Deformation mechanism maps by Frost and Ashby (1982) and Karato (1997) demonstrate that the normalized stress vs. T/T_m plot for a constant grain size of 1mm as well as the normalized stress vs. normalized grain-size plot at a fixed $T/T_m = 0.7$ allow both: power-law creep or Newtonian creep. For the sake of simplicity, we use therefore a Newtonian creep law for the whole mantle inclusive of the crust.

Table 1. Parameters for eq (2.13). D_{cn} is the depth of the lithosphere.

| λ | depth range (km) .. (km) | $k_{2\lambda}$ (dim.less) | $T_{mo\lambda}$ (K) | $\rho_{o\lambda}$ ($kg\ m^{-3}$) |
|-----------|-----------------------------|------------------------------|------------------------|---------------------------------------|
| 0 | 0 .. D_{cn} | 16.7 | 2163 | 3222 |
| 1 | D_{cn} .. 410 | 16.7 | 2163 | 3222 |
| 2 | 410 .. 660 | 16.7 | 2073 | 3310 |
| 3 | 660 .. 771 | 16.7 | 2564 | 4108 |
| 4 | 771 .. 2891 | 16.7 | 2564 | 4108 |

Now, we want to direct our attention to the *first* two factors of the right-hand side of eq (2.13). The necessary parameters of the mantle shells have been collected in Table 1. The quantity $T_{mo\lambda}$ for $\lambda = 3$ and 4 is given by the indirectly deduced zero-pressure melting temperature of orthorhombic perovskite, $MgSiO_3$ (Poirier, 1988). Ohtani (1983) found similar values. Anderson (1995) emphasized that silicate perovskite is a Debye-like solid. Therefore the mathematical treatment can approximately be that one of a monatomic cubic solid which is one of the assumptions for the deduction of Lindemann's law. The zero-pressure density of $MgSiO_3$ perovskite by Ito and Matsui (1978) has been accepted as $\rho_{o\lambda}$ for $\lambda = 3$ and 4.

Using eq (2.1) and PREM, we found rather high K'_0 values for the transition layer. Because of this result of us and the reasoning by Karato (1995, see especially his Figs. 3, 7 and 8), we guess that it is more likely that the transition layer ($\lambda = 2$) has a piclogitic composition with 50-80 % garnet than a pyrolitic composition with 20-40 % garnet (Ringwood, 1991). It is unclear if we should express it so firmly. However, for $\lambda = 2$ we took the pyrope density (Anderson, 1995) for $\rho_{o\lambda}$ and the zero-pressure melting temperature of pyrope (Poirier, 1991) for $T_{mo\lambda}$. The exact values of them are of no great importance. If the garnets dominate the flow behaviour of the transition layer, than we must reckon with a considerably higher transition-layer viscosity, higher than that of the asthenosphere and of the uppermost part of the lower mantle: At equal conditions, garnets have considerably higher shear viscosities than olivine, spinel, perovskite and magnesiowstite (Karato, 1995, 1997). The bcc packing of the garnets points to the applicability of Lindemann's law to the transition layer. The opinions on the viscosity of the transition layer differ. It is true that Ranalli (1998) excludes a low -viscosity transition layer but he suggests that a viscosity maximum exists in the transition layer only for the layered-convection case.

Assuming that forsterite is dominating for the rheology of the asthenosphere, we choose the $T_{mo\lambda}$ of forsterite (Poirier, 1991) for $\lambda = 1$ (and for the sake of simplicity also for $\lambda = 0$) and for $\rho_{o\lambda}$ the density of forsterite (Anderson, 1995), respectively. The value of $k_{2\lambda}$ can be traced back to Karato (1989).

Finally, we replace the melting temperature $f_2 T_{mo\lambda}$ in eq (2.13) by T_{mzb} for the depth range between 771 km and 2891 km, where $T_{mzb} = 3330$ K for 771 km depth and $T_{mzb} = 8000$ K for 2891 km depth. The values in between have been received by linear interpolation. This treatment is justified by the experimental melting temperature curve of (Mg, Fe)SiO₃ - perovskite (Zerr and Boehler, 1993, 1994; Boehler, 1997). Already Van Keken and Yuen (1995) used the mentioned melting temperatures in order to estimate the lower-mantle viscosity, where the whole assumed relation $\eta(T_m)$ was more simplified. It is remarkable that in the model presented here, K3A, the eq (2.13) applies uniformly from the core-mantle boundary to the surface of the continent. Only the 80 km thick oceanic lithosphere has a constant viscosity, namely 5×10^{22} Pa·s, and, as in Walzer and Hendel (1999), the small spreading zone and the small subduction zone have the lowest viscosity value of the oceanic asthenosphere. Except for that, these zones as well as the oceanic plates and the continental lithosphere move unconstrained according to the system of conservation equations and the initial and boundary conditions. As usual in papers on mantle convection, we introduce a limitation of the viscosity range for numerical reasons:

$$10^{-4}\eta_0 \leq \eta \leq 10^{+4}\eta_0 \quad (2.14)$$

Values lying beneath the lower limit will be put on the lower limit, values situated above the upper limit will be set on this upper limit. The quantity

η_0 is determined from

$$\ln \eta_0 = \left\langle \ln \eta_{0\lambda} + \frac{k_{2\lambda} \cdot f_2(x_3) \cdot T_{m0\lambda}}{T_{st}(x_3)} \right\rangle \quad (2.15)$$

since at the beginning of the evolution, the volatile depletion of the primordial mantle did not start and because we assume neither a cold accretion nor an over-hot accretion of the Earth. Walzer and Hendel (1997) gave the reasons for that assumption. Therefore we take the temperature estimate by Stacey (1992) as an initial temperature profile. The angle brackets, $\langle \rangle$, mean the average over all grid points. Further remarks on viscosity follow in Section 3. The algorithms of chemical differentiation and of the local marker refresh can be found in the subsections 2.3 and 2.4 of Walzer and Hendel (1999). The assumed viscosity distribution of the mentioned paper is essentially simpler and more abstracted from the real Earth's mantle.

A systematic variation of the parameters of the presented model K3A has been done, especially a variation of the viscosity factor $\eta_{o\lambda}$ (cf. Appendix B). We introduced a further variation: In a new model variant, K3B, we ignore the knowledge of the perovskite melting curve by Zerr and Boehler (1993, 1994) and we calculate the viscosity of the lower mantle using PREM in the same manner as for the upper 771 km of the mantle in the case of model K3A. Some results are shown by Figs. 10 to 13. We discuss these results in the Section 3.4. The result is that the main features and the principal mechanism are essentially unchanged.

2.4 Fluid dynamics and chemical fractionation

It is a characteristic feature of the present mantle-evolution model that it is no parameterized model. On the contrary, we iteratively solve the conservation equation of *momentum*

$$\begin{aligned} 4 \frac{\partial^2}{\partial x_1 \partial x_3} \left[\eta(T, T_m(P), D') \frac{\partial^2 \psi}{\partial x_1 \partial x_3} \right] + \\ + \left(\frac{\partial^2}{\partial x_3^2} - \frac{\partial^2}{\partial x_1^2} \right) \left[\eta(T, T_m(P), D') \cdot \left(\frac{\partial^2 \psi}{\partial x_3^2} - \frac{\partial^2 \psi}{\partial x_1^2} \right) \right] = \\ Rq \left(1 + \sum_{k=1}^2 P_k \frac{d\Gamma_k}{d\pi_k} \right) \cdot \frac{\partial T}{\partial x_1} \end{aligned} \quad (2.16)$$

and of *energy*

$$\frac{\partial T}{\partial t} + \frac{\partial \psi}{\partial x_3} \cdot \frac{\partial T}{\partial x_1} - \frac{\partial \psi}{\partial x_1} \cdot \frac{\partial T}{\partial x_3} = \frac{\partial^2 T}{\partial x_1^2} + \frac{\partial^2 T}{\partial x_3^2} + H(x_1, x_3, t) \quad (2.17)$$

where the non-dimensional form is given and all non-Boussinesq effects are neglected. Because of eq (2.18), the last two equations contain already the conservation of *mass*. The occurring quantities are explained below in this Section.

The system is completed by the equations of chemical differentiation of the oceanic plateaus and the complementary depleted mantle. The latter equations guarantee the conservation of *four numbers of nuclei*: that for ^{238}U plus ^{206}Pb , ^{235}U plus ^{207}Pb , ^{232}Th plus ^{208}Pb , ^{40}K plus ^{40}Ar . The corresponding procedure has been described in Section 2.3 of Walzer and Hendel (1999).

The essential features of the system are 1) that the non-dimensional specific heat production H evolves from an initially homogeneous distribution of the heat-producing elements in the mantle to an increasingly inhomogeneous distribution. We obtain the result that the homogenizing effect of the convection is not sufficient to compensate the effect of chemical differentiation. 2) We took into account the full dependence of the viscosity, η , on the temperature, T , which depends on the time, t , and on the location vector and not only on its vertical component, x_3 . Furthermore, the viscosity depends on the melting temperature, T_m , which grows with the pressure, P . Since the surface of the oceanic lithosphere borders always on water whereas the surface of the continent does not so, a degree of depletion of volatiles, D' , has been introduced in order to explain the higher stiffness of the continental lithosphere. So, the viscosity depends also on D' and we have to convert eq (2.13) into a non-dimensional relation which is to be inserted in eq (2.16). 3) A further essential feature of the system is the consideration of the two mineral phase transitions at 410 and 660 km depth.

Now, the details are to be explained. We use dimensional quantities again. Because of the assumption of an incompressible Boussinesq fluid and of two-dimensionality, the vertical component, v_3 , and the horizontal component, v_1 , of the solid-state creep velocity can be expressed by the scalar stream function, ψ .

$$v_1 = \frac{\partial\psi}{\partial x_3} \quad \text{and} \quad v_3 = -\frac{\partial\psi}{\partial x_1} \quad (2.18)$$

where x_1 is the horizontal component, x_3 the vertical component of the location vector. The origin of the two coordinates is in the lower left corner of an aspect-ratio-3 box which represents the mantle. Concerning the radionuclide abundances of the chemical reservoirs, we accept the geochemical results of Hofmann (1988). In the present-day silicate spherical shell of the Earth there are five chemical reservoirs neglecting the small volumes of HIMU, EM1 and EM2. The abundances of the major heat-producing elements of the five reservoirs are given in Table 2. In *this* part of the paper, however, only the primitive mantle with tracer index (1), the continental crust and its preliminary form, the oceanic plateaus, with (3) and the depleted mantle or residuum 1 with tracer index (4) is used. However, the movement of the tracers and their transformations by chemical differentiation have been computed by the help of our dynamical system and are not contained in Hofmann's (1988) paper. Table 3 presents some data on the four major heat-producing isotopes: ν stands for the corresponding radionuclide in the formulae, τ_ν represents the decay time or the 1/e life, $H_{o\nu}$ denotes the specific heat production of the ν th radionuclide 4.55×10^9 years ago, $a_{if\nu}$ is the isotope abundance factor. The specific

heat production results from

$$H = \sum_{\nu=1}^4 a_{\mu\nu} a_{if\nu} H_{o\nu} \exp(-t/\tau_{\nu}) \quad (2.19)$$

If the surrounding rectangle of a grid point contains only tracers of the

Table 2. The abundances $a_{\mu\nu}$ of the major heat-producing elements according to Hofmann (1988)

| Marker Index | (1) | (2) | (3) | (4) | (5) |
|--------------|------------------------|---------------------|-------------------------|-------------|-------------|
| Reservoir | Primitive mantle (ppm) | Oceanic crust (ppm) | Continental crust (ppm) | Res 1 (ppm) | Res 2 (ppm) |
| K | 258.2 | 883.7 | 9100 | 201.48 | 161.98 |
| Th | 0.0813 | 0.1871 | 3.5 | 0.0594 | 0.0529 |
| U | 0.0203 | 0.0711 | 0.91 | 0.0146 | 0.0112 |

Table 3. Data of the major heat-producing isotopes

| Isotope | ⁴⁰ K | ²³² Th | ²³⁵ U | ²³⁸ U |
|----------------------------|------------------------|-------------------------|------------------------|-------------------------|
| ν | 1 | 2 | 3 | 4 |
| τ_{ν} [Ma] | 2015.3 | 20212.2 | 1015.4 | 6446.2 |
| $H_{o\nu}$ [$W kg^{-1}$] | 0.272×10^{-3} | 0.0330×10^{-3} | 47.89×10^{-3} | 0.1905×10^{-3} |
| $a_{if\nu}$ | 0.000119 | 1 | 0.0071 | 0.9928 |

reservoir ν then the abundances $a_{\mu\nu}$ of this special ν determine the dimensional value of H at this grid point. If different tracers are in the surrounding rectangle then the weighted arithmetic mean of these abundances have to be inserted into eq (2.19). The heat production density Q is measured in $W \cdot m^{-3}$. In order to non-dimensionalize Q we define a quantity

$$Q_0 = H_0 \rho_0 \quad (2.20)$$

where ρ_0 is the reference density (cf. Table 4) and H_0 is a special average value of the dimensional H , namely

$$H_0 = \sum_{\nu=1}^4 a_{\mu\nu} a_{if\nu} H_{o\nu} \exp(-t_h/\tau_{\nu}) \quad (2.21)$$

where $a_{\mu\nu}$ are those of the Type 1 tracers and $t_h = (1/2)(4550 \text{ Ma})$. The non-dimensional variables have been introduced in Appendix A. The remaining conversion parameters are given in Table 4. In eq (2.16) a Rayleigh number, Rq , characteristic of the run, and appropriate for heating from within and from below has been used. It is defined by

Table 4. Additional model parameters

| Parameter | Description | Value |
|---------------|--|---|
| h | Depth of the convecting layer | 2.891×10^6 m |
| h_1 | Depth of the exothermic phase boundary | 4.10×10^5 m |
| h_2 | Depth of the endothermic phase boundary | 6.60×10^5 m |
| g | Mean gravitational acceleration in the mantle | 9.94 m s ⁻² |
| ρ_0 | Reference density | 3340 kg m ⁻³ |
| c_p | Specific heat at constant pressure | 1000 J kg ⁻¹ K ⁻¹ |
| κ | Thermal diffusivity | 10^{-6} m ² s ⁻¹ |
| q_{cmb} | Heat flow at the core-mantle boundary | 0.02 W m ⁻² |
| t_h | Half of the time span of the Earth's evolution | 2275 Ma |
| α | Coefficient of thermal expansion | 3.14×10^{-5} K ⁻¹ |
| γ_1 | Clapeyron slope for the olivine-spinel transition | $+3 \times 10^6$ Pa K ⁻¹ |
| γ_2 | Clapeyron slope for the spinel-perovskite plus magnesiowüstite transition | -4×10^6 Pa K ⁻¹ |
| f_{a1} | Non-dimensional density jump for the olivine-spinel transition | 0.08 |
| f_{a2} | Non-dimensional density jump for the spinel-perovskite plus magnesiowüstite transition | 0.10 |
| d_1 | Non-dimensional transition width for the olivine-spinel transition | 0.05 |
| d_2 | Non-dimensional transition width for the spinel-perovskite plus magnesiowüstite transition | 0.05 |
| η_{lith} | Viscosity of the oceanic lithosphere | 5×10^{22} Pa s |
| η_{thr} | Threshold viscosity | 2.1×10^{20} Pa s |

$$Rq = \frac{\rho_0 \alpha g h^3}{\kappa \eta_0} \cdot \frac{(Q_0 h + q_{CMB}) h}{k} \quad (2.22)$$

where the thermal conductivity k is defined by

$$k = \kappa c_p \rho_0 \quad (2.23)$$

The second big factor on the right-hand side of eq (2.22) replaces the constant temperature difference of the Bénard case. Since we want to include the thermal evolution of the mantle, the Bénard case would not be appropriate for that purpose.

This seems to be a suitable place to introduce the *boundary conditions*. Because of the long existence of fluviatile sediments, the average surface temperature of the Earth must have been between 0°C and 100°C since at least 3.8×10^9 years. The real boundaries were probably narrower, yet. Therefore we assume a constant surface temperature, say 288 K, for the modeling of the endogene evolution. Since the solar luminosity grew by 26 % in the course of 4.57×10^9 years, the mentioned geological observation is on no account insignificant. It is probably the global carbon cycle, particularly the slow decrease of the CO₂ content of the air by sedimentation of limestone and dolomite, which causes this approximate temperature constancy. On the other

hand, for the core-mantle boundary (CMB) no such thermostatic mechanism is known. From investigations of komatiites we know that the mantle temperature decreases by 100 K during about 1000 Ma. In model K2A (Walzer and Hendel, 1999), the theoretical Earth's mantle cools down by 400 K during the last 3700 Ma. For these two reasons, the laterally averaged CMB temperature probably decreases, too, at least for the last 3700 Ma. Therefore, regarding the *time* dependence, a constant CMB temperature boundary condition would be a less good approach for an evolution model of the mantle's last 4490 Ma. Concerning the *lateral* dependence it is possible that the dependence of the real CMB temperature on x_1 nearly vanishes because the outer core has high electrical and thermal conductivities and a hydromagnetic convection with relatively high flow velocities. In anticipation of our description of the results of K3A, it may be pointed out that the last three panels of Fig. 3 show isolines of 4444 K which run nearly parallel to the CMB. Lister and Buffett (1995) computed the dynamo efficiency in terms of a Carnot-style redistribution of heat and mass in the outer core. The corresponding results made us realize that the CMB heat flow density would be $17.74 \text{ mW}\cdot\text{m}^{-2}$. In his Section 6.7.5 entitled Constancy of the Core-to-Mantle Heat Flux, Stacey (1992) emphasizes this constancy since the inner core growth and the dynamo mechanism must be *simultaneously* possible. Based on the heat transport of mantle plumes, Sleep (1990) concluded that the CMB heat flow is $3.0 \times 10^{12} \text{ W}$ corresponding to a heat flow density of $19.7 \text{ mW}\cdot\text{m}^{-2}$. Therefore it is rather well justified to assume a constant CMB heat flow density, namely $20 \text{ mW}\cdot\text{m}^{-2}$. Apart from that we presume free-slip conditions at the Earth's surface and at the CMB. The vertical side walls have periodic boundary conditions.

The following is intended to explain the definitions of those quantities of the right-hand side of eq (2.16) which are connected with the *mineral phase transitions* in 410 and 660 km depth. The definitions of Table 4 should be used as a complement. The relationship

$$P_{tk} = P_{ok} + \gamma_k T \quad (2.24)$$

shows the dependence of the transition pressure, P_{tk} , on the temperature, T . For a positive (negative) Clapeyron slope P_{tk} , grows (decreases) with T . The quantity P_{ok} , is the transition pressure for vanishing temperature. The excess pressure, π_k , is a result of

$$\pi_k = P - P_{ok} - \gamma_k T \quad (2.25)$$

The density, ρ , depends not only on the temperature but also on the density contrasts, $\Delta\rho_k$, at the phase-transition planes:

$$\rho = \rho_0 \left(1 - \alpha T + \sum_{k=1}^2 \Gamma_k \Delta\rho_k / \rho_0 \right) \quad (2.26)$$

where

$$\Gamma_k(\pi_k) = \frac{1}{2} \left(1 + \tanh \frac{\pi_k}{d_k} \right) \quad (2.27)$$

is a smoothed step function. $\Gamma_k = \Gamma_k(P, T)$ serves as a measure of the relative fraction of the heavier phase. If the non-hydrostatic part of the pressure is neglected then

$$\frac{d\Gamma_k}{d\pi_k} = \frac{1}{2d_k} \left(1 - \tanh^2 \frac{\pi_k}{d_k} \right) \quad (2.28)$$

applies where the maximum of the curve is at $\pi_k = 0$. We insert

$$\pi_k = (h - h_k)/h - x_3 - \gamma_k T \quad (2.29)$$

for $k = 1$ and 2 . The eqs (2.24) to (2.29) have been introduced in a similar form by Christensen and Yuen (1985). Eq (2.27) can be traced back to Richter (1973). Finally, we receive the phase buoyancy parameter, P_k , from

$$P_k = \frac{Rb_k}{Rq} \gamma'_k \quad (2.30)$$

and

$$Rb_k = \frac{gh^3 \rho_0}{\kappa \eta_0} f_{ak} \quad (2.31)$$

with

$$f_{ak} = \Delta \rho_k / \rho_0 \quad (2.32)$$

Eq (2.16) contains both, the buoyancy due to heating by radioactive decay and the buoyancy of the thermally induced distortion of the phase boundaries at 410 and 660 km depth. Contributions which vanish with vanishing dissipation number have been neglected. So, non-Boussinesq effects are excluded.

Since the existence of partial melt is a prerequisite for *chemical differentiation*, the temperature must come right up to the nominal melting temperature. Therefore the viscosity falls below a threshold value, η_{thr} . If, in addition, the asthenosphere is enriched in that region so that it has a higher percentage of incompatible elements than the MORB source, then the volcanism generates the oceanic plateaus which are enriched in comparison with normal oceanic MORB crust. The translation into our model reads as follows: If in the beginning the relatively hot area was full of Type 1 tracers or if enough new Type 1 tracers are subsequently supplied by upwelling plumes from the lower mantle then the Type 1 tracers will be transformed into Type 4 tracers in that hot area. The released amount of radionuclide material is instantaneously assigned to the tracers in the lithospheric part which is situated above. This is done so that the mentioned four numbers of nuclei are conserved. In this way the Type 3 tracers are generated. The instant change is justified since silicate liquids rise more quickly by far in comparison with the solid-state creep in the asthenosphere. The generated unconnected Type 3 tracers are horizontally carried with the flow. Near the downwelling area they will be accreted to the continent which consists of Type 3 tracers moving en bloc. The mechanism

has been described in Section 2.3 of Walzer and Hendel (1999). So, in our models we did not simply put a continent on the mantle but the continent develops as outlined above. However, the viscosity theories of the two models are very different.

3 Results and discussion of the convection-fractionation models K3A and K3B

3.1 General description of the results of K3A and comparison with observational results

In the following the results of the first new 2-D model, K3A, are represented by pictures. After a short discussion of our own picture we compare each result with observations or theoretical results of other authors. The laterally averaged heat flow at the Earth's surface as a function of age is depicted in the first panel of Fig. 1, to be exact the heat flow density in $\text{mW}\cdot\text{m}^{-2}$. The upper curve denotes the laterally averaged oceanic heat flow, q_{obo} . The curve of the average surface heat flow of the total Earth, q_{ob} , runs along the q_{obo} curve slightly deeper whereas the curve of the average continental heat flow, q_{obc} , shows distinctly lower values for the most epochs. This is essentially in coincidence with the present-day heat-flow values of Pollack et al. (1993). Analysing 24774 observations from heat flow measurements, they have got an average ocean-bottom heat flow of $101 \text{ mW}\cdot\text{m}^{-2}$, a total surface heat flow of $87 \text{ mW}\cdot\text{m}^{-2}$ and an average continental surface heat flow of $65 \text{ mW}\cdot\text{m}^{-2}$. So the curves of the first panel of Fig. 1 reflect the right order of magnitude and the general tendency toward a lower continental heat flow. The present-day q_{ob} , corresponds rather well with the $87 \text{ mW}\cdot\text{m}^{-2}$ by Pollack et al. (1993), only a separation of the three curves is not visible for the present day.

Preparing the discussion of the second panel of Fig. 1, we introduce some geological findings of other authors: Now only a few research workers hold the viewpoint that the whole material of the continental crust evolved in the early Archean and that every later continental accretion is palingene (Armstrong, 1991). The contemporary growing consensus consists in the conclusion that the total mass of all continents increases episodically over the whole history of the mantle (see e.g. Taylor and McLennan, 1995; Abbott et al., 1997). However, the opinions differ with respect to the chemical composition of an averaged continental crust. Taylor and McLennan (1995) are of the view that the averaged continental crust has an andesitic composition and that the continent grows by addition of island arcs of the mentioned composition whereas Abbott et al. (1997) concluded that the total continental mass increases by the accretion of oceanic plateaus, hotspot tracks and only to a minor degree of island arcs. We fall in with the latter views in this paper: In the second panel of Fig. 1, the previously described conversion of markers (or tracers) has been computed as a function of age. Hence, the panel shows the generation of

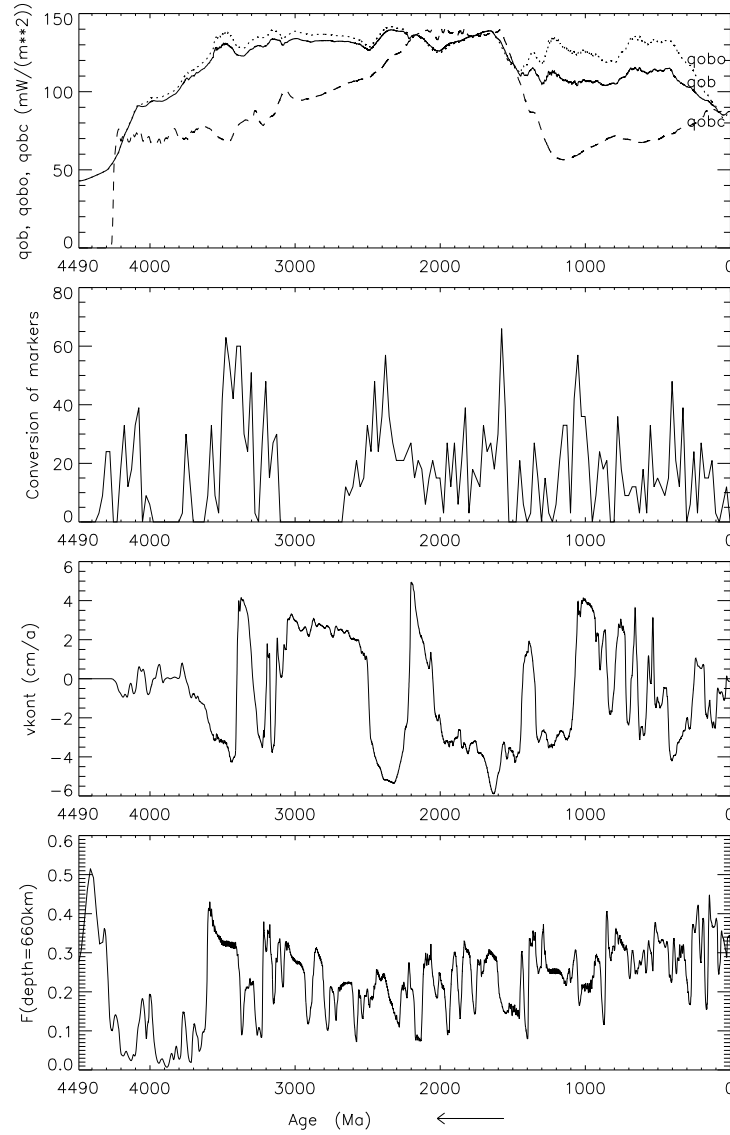


Fig. 1. The evolution of the present 2-D Earth's mantle model, K3A, presented by some relevant characteristic quantities as a function of the age. First panel, upper curve: laterally averaged ocean bottom heat flow, q_{obo} . First panel, middle curve: laterally averaged heat flow at the solid surface of the whole Earth, q_{ob} . First panel, lower curve: laterally averaged continental-surface heat flow, q_{obc} . Second panel: number of newly produced Type 3 tracers per 25 Ma. This curve represents the evolution of the juvenile continent material. Third panel: drift velocity of the continent. Fourth panel: vertical mass flow through the 660-km phase boundary.

continental material as a function of age. The differentiation process is indeed episodically distributed over the whole time axis. About 40 % of the continental material has been produced in the model Archean. Rudnick (1995) estimated from a lot of Sm-Nd investigations that 35-60 % of the present continental mass was originally generated in the Archean.

The third panel of Fig. 1 shows that the model continent moves as a raft first to the left then to the right etc, that the right order of magnitude of the drift velocity has been computed and that there are time spans of higher and lower lateral continental velocity. Of course, in time spans of high continent velocity it is more probable that free Type 3 tracers accrete to the model continent so that, in our simple model, orogenesis is unsteady distributed over the time axis. This corresponds with observations on the real Earth.

In the last panel of Fig. 1, the vertical mass flow function, F , through the 660-km discontinuity is shown as a function of age where

$$F = \frac{\left[a^{-1} \int_0^a v_3^2(x_1, x_3) dx_1 \right]^{1/2}}{\left[a^{-1} \int_0^a \left[\int_0^1 (v_1^2(x_1, x_3) + v_3^2(x_1, x_3)) dx_3 \right] dx_1 \right]^{1/2}} \quad (3.33)$$

where a is the aspect ratio of the box. This definition has been used also by Steinbach and Yuen (1992). Also this flow through proves to be episodic. Altogether the four panels of Fig. 1 seem to be rather realistic.

The same can be said about Fig. 2, the upper panel of which shows the mantle average of the heat production density, \bar{Q} as a function of the age. According to expectation an approximately exponential decrease is to be seen. The lower panel of Fig. 2 contains the fluctuations of the Nusselt number, Nu , as a function of age. The model Nu has Earth-like magnitudes.

3.2 Temperature and viscosity: results and comparison with the results of other researchers

Fig. 3 depicts four snapshots of the temperature distribution in the mantle, the first of which is for a time in the Archean. The second snapshot is situated in the Proterozoic, the third one in the Paleozoic. The lower panel represents the geological present. Reddish stands for hot, the colder parts of the mantle are green or even blue. In the panels of all the four times, the moderate heating from below generates a thin hot layer immediately above the CMB. Instabilities cause the rise of hot material. The hot stream is dammed up by the high-viscous transition layer. Hot material is collected beneath the transition layer. The four viscosity snapshots of Fig. 4 show that a second low-viscosity layer was created in that way. In spite of it we want to emphasize that the system is essentially heated from within. The four viscosity distributions of Fig. 4 are shown for the same times as the temperature distributions of

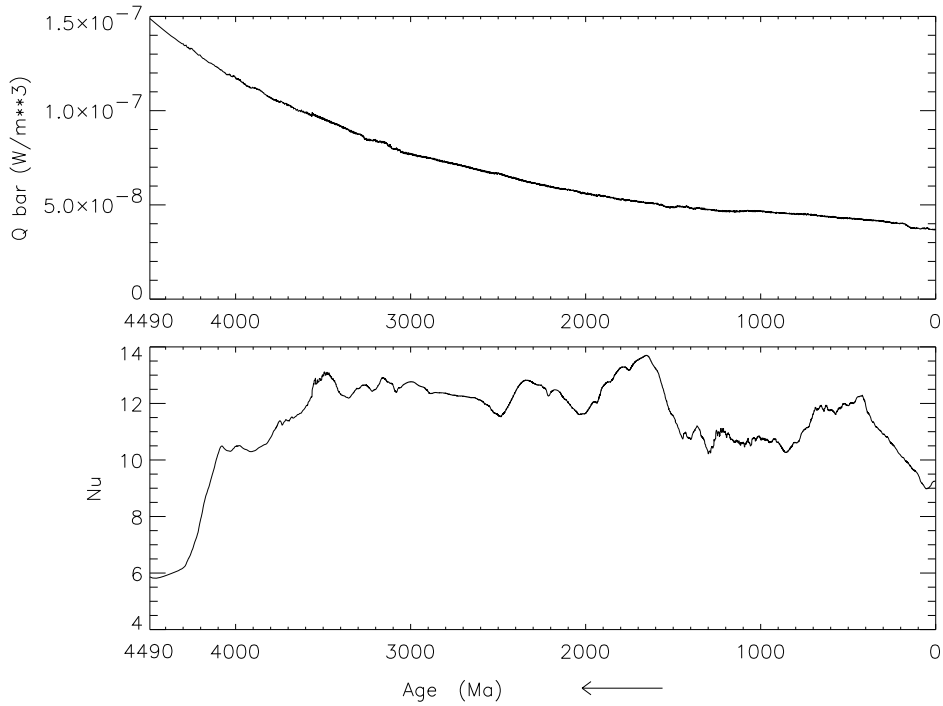


Fig. 2. Two quantities as a function of age. Model K3A. First panel: the heat production density, averaged over the whole mantle, \bar{Q} . Second panel: the Nusselt number, Nu .

Fig. 3. In Fig. 4 red denotes areas of low viscosity whereas blue and black colors represent areas with high and very high viscosity, respectively. *The most striking feature is that the transition layer is a distinctive high-viscosity zone in all epochs.* However, this high-viscosity layer can occasionally be penetrated from below or from above. It turned out that a relatively high viscosity exists also in the lower part of the lower mantle except the D'' layer. If a plume breaks through this high-viscous part of the lower mantle then the vertical pipe remains nearly permanent on the spot. The lateral movement of the plume is considerably slower than the lateral movement of the continent. So, also in the *model* the *plumes* are a relatively fixed *reference frame* to record the continental movement.

Fig. 5 depicts the vertical mass flow as a function of depth for the geological present. Because of the high transition-zone viscosity in the last panel of Fig. 4, the low flow through that layer is comprehensible. But the flow through is absolutely not zero. As expected, the vertical mass flow through the lower part of the lower mantle is also low. The laterally averaged viscosity as a function of depth is especially interesting (see Fig. 6). The figure demonstrates that one may *not use an unchangeable viscosity profile* in order to compute the mantle's

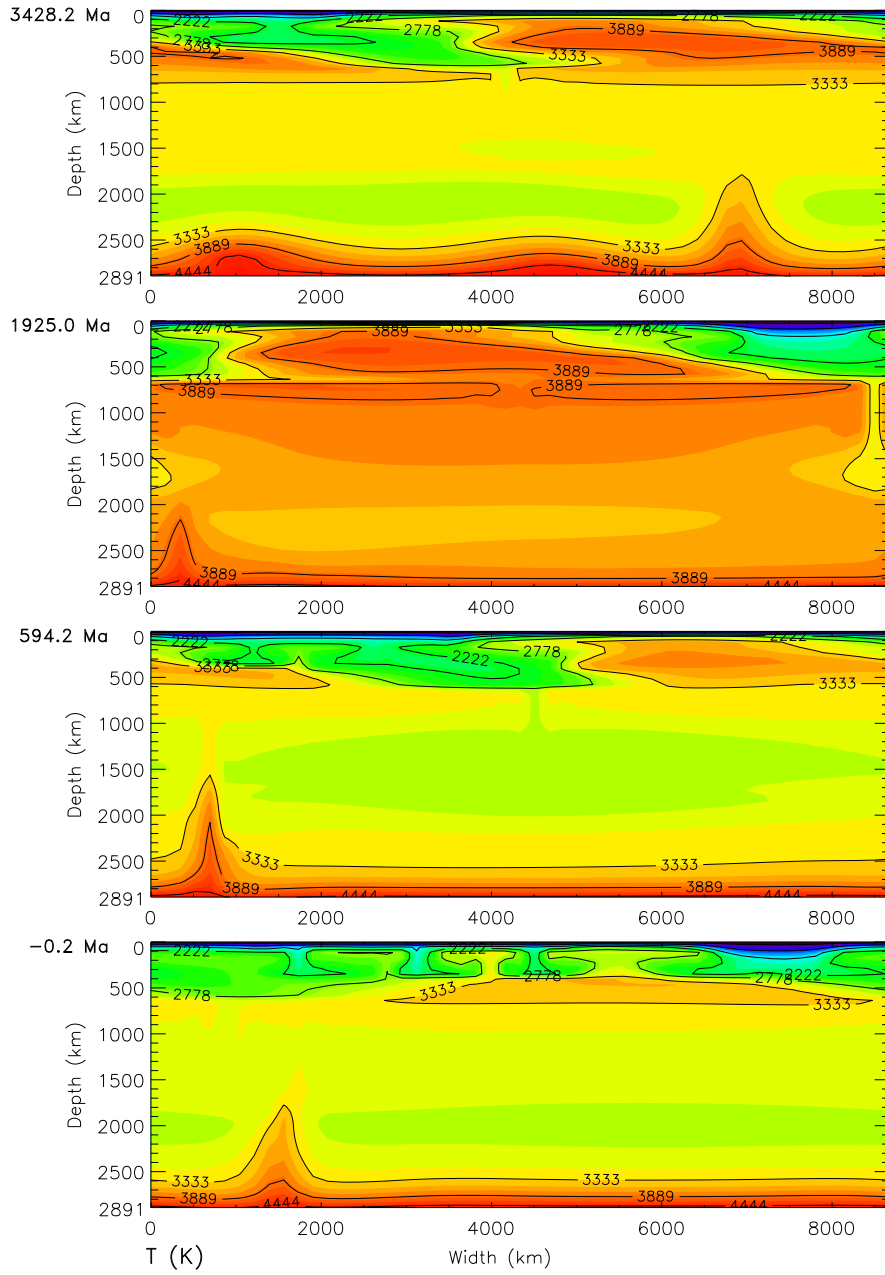


Fig. 3. The temperature, $T(x_1, x_3)$. Model K3A. The ages of the snapshots are given at the upper left corner of each panel.

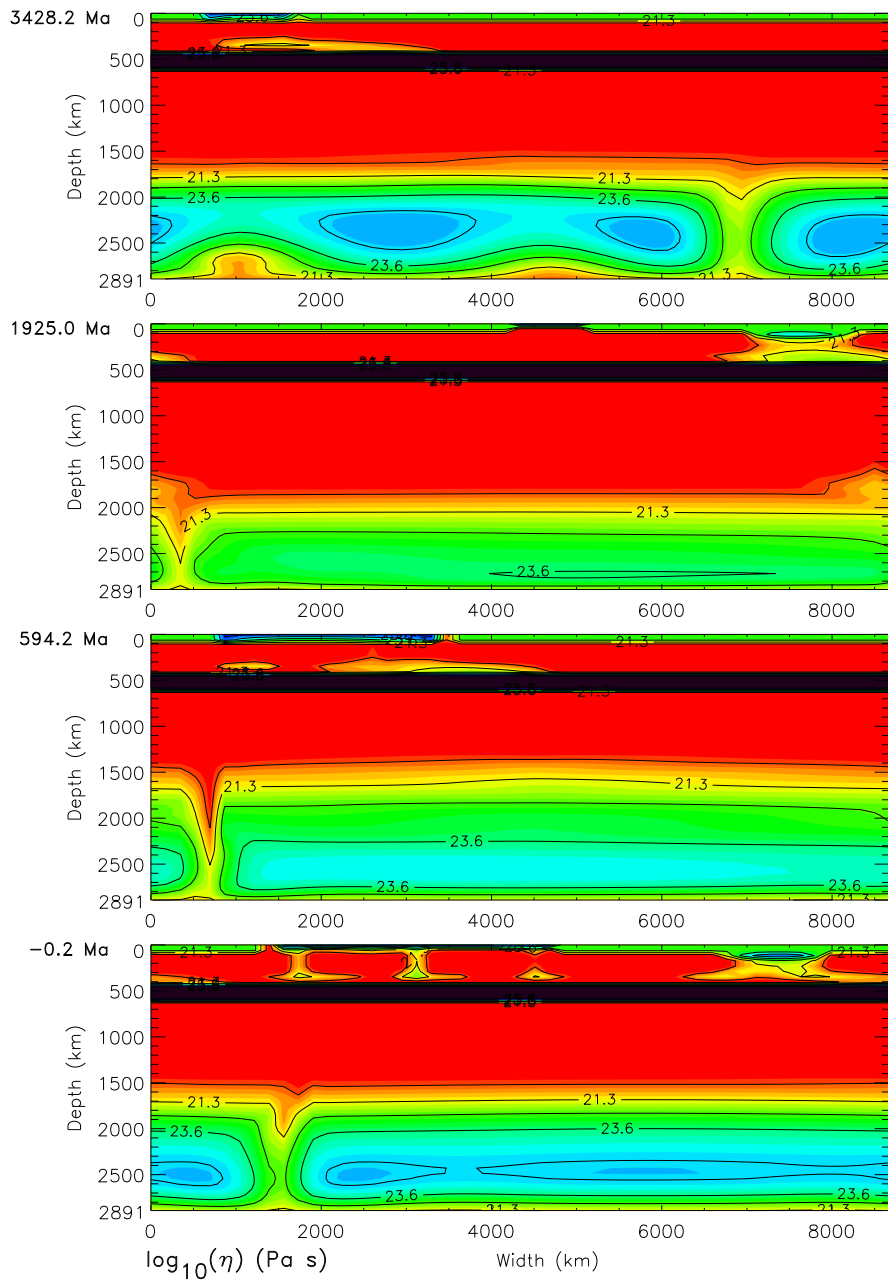


Fig. 4. The evolution of the viscosity of K3A is represented by a series of snapshots. The ages are given at the upper left corner of each panel. The curves are lines of equal logarithm of viscosity in Pa.s.

evolution. We suspect that the transition-layer viscosity is somewhat too high because in the corresponding $\partial K/\partial P$ values of PREM some additional phase transitions can be hidden. But probably a correction would not change the character of a pronounced maximum. The necessary information for such a correction is not yet available.

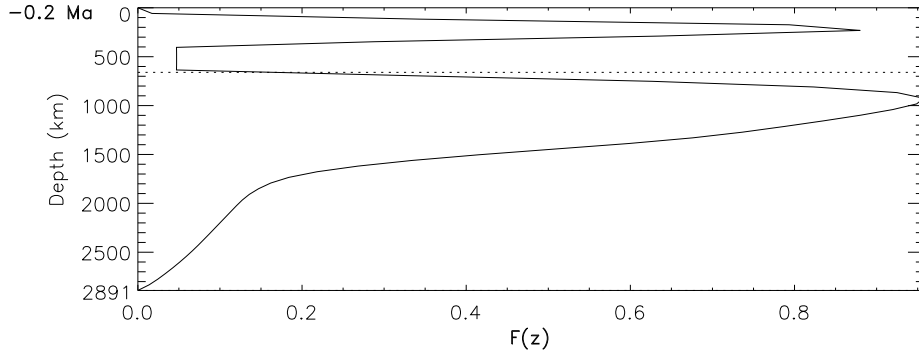


Fig. 5. The vertical mass flow function, F , as a function of depth virtually for the present time of the model K3A.

We wonder whether there are indications of such a viscosity distribution as in the Figs. 4 and 6 from other workers. Kido and Čadek (1997) and Kido et al. (1998) investigated intermediate degrees of the oceanic geoid ($l = 12 - 25$) and the tomographic structure below the Pacific, Atlantic, and Indian Oceans in order to find the radial viscosity structure of the upper half of the mantle. They confined themselves to that huge oceanic area which is relatively low disturbed in order to exclude problematic masses beneath the subduction zones and beneath the continents. The correlation of the predicted geoid with the observed one over the mentioned area has been taken as the fitting function in a genetic algorithm approach. They used 100 starting profiles which have been iterated for 100 generations. In nearly all cases, the wealth of solutions shows not only the well-known asthenosphere between lithosphere and transition layer but a second low-viscosity layer below the transition layer. Fig. 7 demonstrates a typical viscosity structure of this kind. The ubiquitous appearance of these two low-viscosity layers is all the more remarkable since Kido and Čadek (1997) used three different tomographic models of other authors. One of the tomographic models is limited to depths down to 500 km, the most sophisticated one to depths down to 1200 km. In both cases, the seismic tomography has been supplemented down to the CMB by the results of the third model. It is evident that Fig. 7 represents the essential features of the viscosity profile only for the upper half of the mantle since the resolving power is low for the lower half. Fig. 7 agrees with our viscosity profiles in the essential features (cf. Fig. 6) where in our model the transition-layer

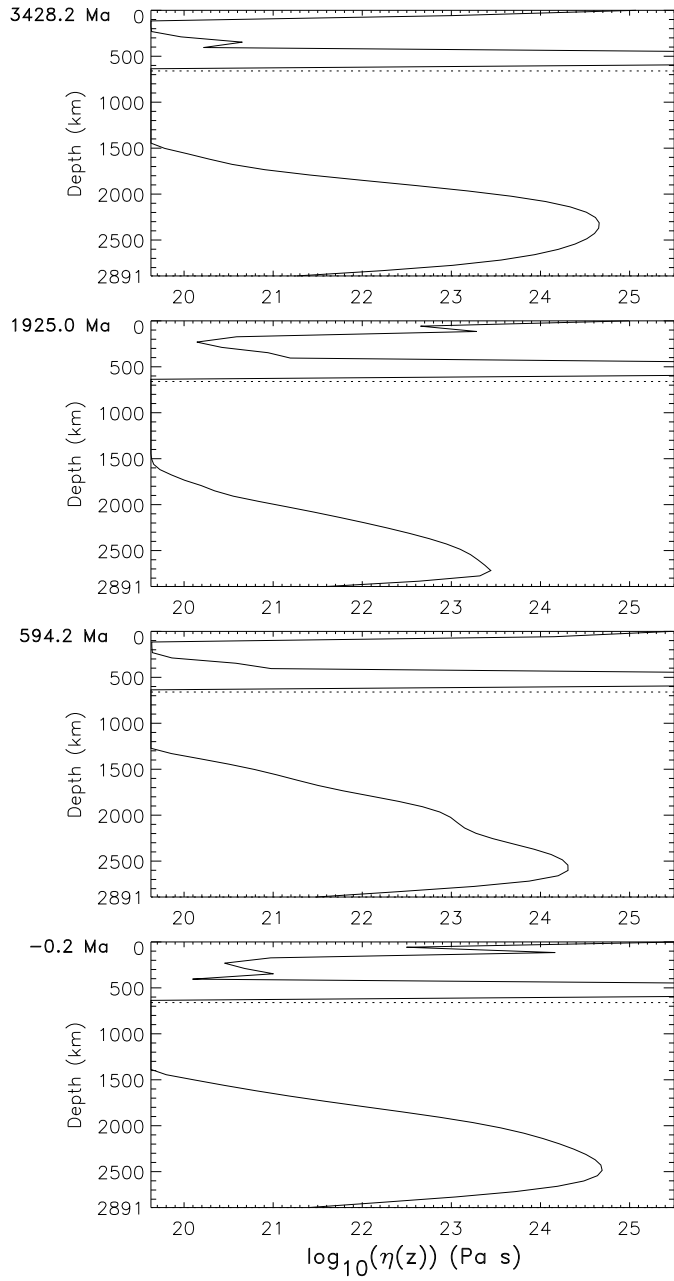


Fig. 6. Four snapshots of K3A. The laterally averaged logarithm of the viscosity is shown as a function of depth. The ages of the snapshots are given at the upper left corner.

viscosity is evidently overestimated since the $\partial K/\partial P$ values of PREM for the transition layer are too high. Nevertheless those viscosity values must be elevated. Therefore the viscosity of the transition layer must be essentially higher than the viscosity of the asthenosphere and of the uppermost lower mantle. Investigating the seismic tomography and the geoid, already King and Masters (1992) concluded that there is a second low-viscosity layer beneath the 660-km discontinuity.

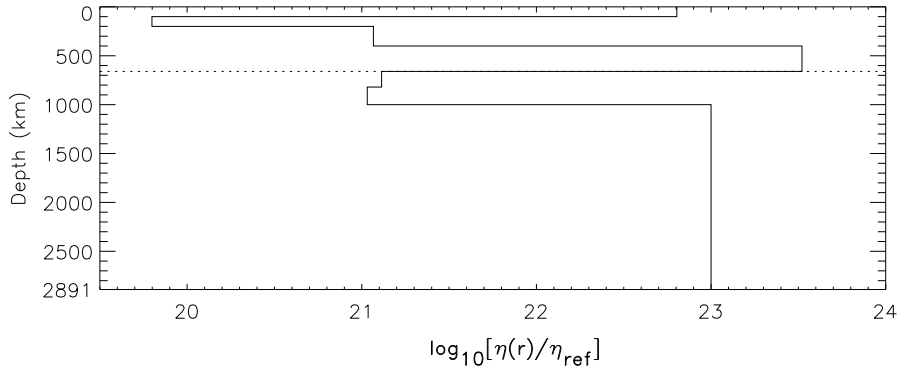


Fig. 7. One of the viscosity profiles which yield the highest penalized correlations. The picture corresponds to run 10 of Fig. 11 by Kido et al. (1998). It has been redrawn using numerical values kindly provided by Kido.

Cserepes and Yuen (1997) used these findings to investigate the convection in a 3-D box. They neglected the 410-km phase transition, internal heating and the complex dependence of the viscosity on temperature. The ascend of the viscosity curve with the pressure has been modelled only for the lower mantle presumably under the influence of Zerr and Boehler (1993, 1994). Assuming a purely depth-dependent viscosity distribution which nevertheless has many features in common with our viscosity distribution (cf. Figs. 4 and 6), they received a tendency of the system toward layering. We can corroborate this finding for our system although we installed the (P,T)-dependence of the viscosity, *both* phase boundaries at 410 and 660 km depth and the dominating heating from within and although we made 2-D computations. Apart from it we take into account the evolving inhomogeneity of the internal heating, which develops by chemical differentiation. Our system is slightly leaky, that is, in spite of the high-viscosity transition layer a restricted material transfer is taking place between the upper mantle and the lower mantle. This is also necessary for geochemical reasons. Both investigations complement each other rather well because the system by Cserepes and Yuen (1997) easily allows to discuss the physical mechanism whereas it is our essential aim to produce a somewhat realistic dynamical image of the chemical and thermal evolution of

the mantle. The dynamical consequences of a radial mantle-viscosity distribution with two low-viscosity layers has been discussed by Yuen et al. (1998), too. They found that there is a tendency to double-layer convection and that many small-scale plumes can rise from the transition zone. We received secondary plumes in some runs, too.

Čadek and van den Berg (1998) made a dynamical modelling of the geoid and investigated the radial profile of the mantle temperature. For each of the models they found the rheological parameters by fitting the geoid. Because the inversion is non-unique (see also Pari and Peltier, 1998), they derived two different forms of a curve for the radial dependence of the mantle viscosity. One group of it (their C and D) is similar to our Fig. 6. The essential difference is that our profiles alter as a function of time where, however, the type is conserved. Similar to our Fig. 6, Type C/D has a stiff lithosphere. Beneath of it there is a classical asthenosphere. In our model it extends down to 410 km but in C/D somewhat deeper. Our second viscosity maximum is situated in the transition layer according to PREM whereas the second peak of the C/D curve is between 660 and 800 km depth. The second low-viscosity layer of C/D has its minimum value between 800 and 1000 km depth. That is in approximate coincidence with our Figs. 4 and 6. For C/D, the broad viscosity maximum of the lower mantle is between 2000 and 2500 km depth. In our Fig. 6, the peak is between 2400 and 2500 km depth. This depth is slightly age-dependent in K3A. In both models, there is a decrease of the viscosity immediately above the CMB.

In accord with our model, van den Berg and Yuen (1998) use a stiff lower-mantle rheology and a strong pressure dependence of the viscosity in the lower mantle. Unlike van den Berg and Yuen (1998), we keep the heat flow at the CMB constant since we intend to model all of the time of the mantle evolution and because we expected that the average temperature of the mantle decreases during the longest time span of the Earth's evolution. So, it was probable that the laterally averaged CMB temperature also decreases as a function of time. Both expectations are fulfilled by model K3A. However, van den Berg and Yuen (1998) investigated the effects of rheological layering on the mantle heat transport. So, it was legitimate to use the CMB temperature as a control parameter. According to expectation, they received a strong decrease of the viscosity as a function of depth from a maximum in the lower part of the lower mantle toward the CMB. Furthermore, van den Berg and Yuen (1998) found that the viscosity hill in the lower part of the lower mantle moved downward with increasing internal heating. This is in accordance with the four panels of our Fig. 6. In the last three panels, the maximum of the hill moved upward in direction to the surface since the internal heating is decreasing and the maximum lower-mantle viscosity value grows with time since the average mantle temperature decreases in this time span. The first panel is influenced by the initial evolution but if we regard its temperature distribution then we find absolutely the same behavior.

Among the viscosity papers which are based on the geoid there are also deviating models, e.g. that of Pari and Peltier (1998). Therefore, we want to point out the good consistence of our model with papers on solid-state physics and mineralogy. It is generally acknowledged that there are phase transitions in 410 and 660 km depth and that there the lattice and the physical parameters quickly alter with depth. It would be strange to expect that the activation energy and the activation volume of the different creep mechanisms does not alter at the corresponding depth. Since both quantities are in the exponent of the viscosity law there should be a jump in the viscosity. Of course, also the mineralogical mixture of the transition layer influences the viscosity of it. For pyrolyte, the 20-40 % of garnet do not dominate the rheology; for piglogite, the 50-80 % garnet would make the transition layer rather tenacious (Weidner, 1986; Karato et al., 1995). Ringwood (1990) emphasized that the garnet content grows with depth and that there are more than 90 % garnet at the bottom of the transition layer. Karato (1997) stressed that the normalized creep strength of garnet is an order of magnitude or more higher than that of olivine, perovskite and spinel for the expected T_m/T -regions. The most experiments have been made in the power law creep regime. If the creep is diffusion-controlled then a difference in the diffusion coefficient of about 10^3 can be expected (Karato et al., 1995). The ten kinds of garnets, which have been investigated by the mentioned authors, had high strength for high temperatures as well as for low temperatures. Therefore, also other physical and mineralogical authors consider it possible that the transition layer has an elevated viscosity, augmented in comparison to the neighboring layers. However, the real Earth consists of polyphase materials and there is a considerable influence of volatiles (H_2O , CO_2 , CH_4 ,...) on the viscosity (Drury and Fitz Gerald, 1998). So, we have a certain factor of uncertainty in our considerations. However, Stixrude (1997) emphasized that the total width of a phase transition can be essentially reduced by the presence of non-transforming phases. It is well-known that the seismologically observed discontinuities at 410 and 660 km depth are much too sharp. So, they cannot be explained by the phase transition of one pure mineral. Because of detailed reasons by O'Neill and Palme (1998) we are not inclined to introduce jumps in the chemical gross composition in order to explain this sharpness. We think that elastic and other physical quantities (activation energy, activation volume,...) of mixed minerals jump at 410 and 660 km depth. Ranalli (1998) excludes jumps that produce a low-viscosity layer in the transition zone. So it seems that a lot of arguments support Karato's et al. (1995) thesis of a high-viscous transition layer which is situated below the conventional asthenosphere and above a low-viscosity layer in the uppermost parts of the lower mantle.

Here, we want to comment on the paper by van Keken and Ballentine (1999). They used a steady-state viscosity profile whereas the present paper allows the viscosity to evolve with time. We think that it is very meritorious that van Keken and Ballentine (1999) attack the important problem why there are two reservoirs of contrasting $^3He/^4He$ in the mantle. They concluded,

however, that their “models cannot satisfactorily explain the existence of two distinct OIB and MORB $^3\text{He}/^4\text{He}$ sources”. Whether including the effects of phase changes or not, their models show rapid outgassing of the mantle, too rapid in comparison with observation. The time dependence of our viscosity distribution is, on the other hand, an essential feature in order to calculate the evolution of the mantle for the last 4.49×10^9 a. However, we don't think that the steady-state character of the viscosity profiles of van Keken and Ballentine (1999) is the reason for the failure of their models. The introduction of a high-viscosity transition layer could be more helpful. Moreover, it can be that the reasons are hidden in the conception. The following speculation could possibly be a way-out. Metallization of fluid hydrogen occurs at 140 GPa (Nellis, 2000). The CMB pressure is 135.7509 GPa according to PREM. If the accretion of the Earth took place in a gaseous cloud (Hayashi et al., 1985) then metallized hydrogen, ^3He , ^4He and other light components could contribute to lower the density of the outer core since it is well-known that pure iron has a too high density at outer-core pressures. So, the outer core could be a source of primordial ^3He .

3.3 The evolution of the major geochemical reservoirs of the mantle

We made a lot of runs with varying parameters (cf. Appendix B). Fig. 8 represents the result of the evolution of the distribution of incompatible elements for a viscosity parameter $\eta_{o\lambda} = 4.0 \times 10^8$ Pa·s (cf. eq (2.13)). The colors are explained in the figure caption. Qualitatively, we always obtain the same evolution for moderately varying parameters: Sometimes the temperature approaches the generalized melting temperature, T_m , in an area of the uppermost part of the asthenosphere. If, therefore, the viscosity of that area falls below a certain threshold viscosity, η_{thr} , then a certain geochemically determined mass of incompatible elements (U, Th, K, ..) rises to the oceanic plateaus (dark-blue) which will be conveyed by the lateral movement of the oceanic lithosphere to the continent (red). So, the continent grows by accretion. This increase corresponds to geological observations (Taylor and McLennan, 1995; Abbott et al., 1997). Cf. Fig. 1, second panel. The more continent develops the more complementary reservoir, the depleted mantle, grows. The latter one is depicted with yellow to greenish color according to the rising degree of depletion of incompatible elements. Contrary to model K2A (Walzer and Hendel, 1999), the depleted mantle of K3A is mainly confined to the upper mantle since the high-viscosity barrier of the transition layer is a stronger obstacle than the two phase boundaries. In the K2A model, both the phase boundaries and, to a higher degree, the high viscosity in the lower part of the lower mantle cause the conservation of the two principal mantle reservoirs whereas in K3A the transition-layer barrier additionally works against the mixing by convection. Fig. 8 shows that nearly the whole upper mantle is filled now with MORB-source material whereas the corresponding picture of K2A (Fig.9(e))

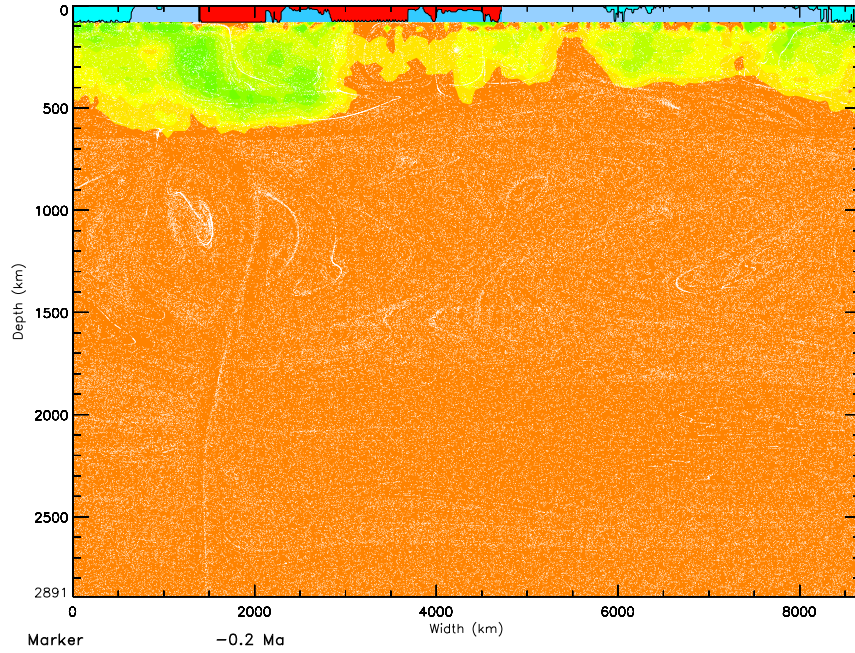


Fig. 8. The result of the evolution of the geochemical reservoirs of K3A. The snapshot is shown for an age of -0.2 Ma. Orange: a mantle area which is abundant in incompatible elements, yet. Yellow to greenish: depleted to strongly depleted mantle area, virtually the MORB source. Red: continental lithosphere. Light-blue: normal oceanic lithosphere. Dark-blue: oceanic lithosphere with oceanic plateaus. Whitish nearly vertical string: plume, rising from CMB.

by Walzer and Hendel, 1999) shows an additional depletion in the upper third of the lower mantle. The computational algorithm for getting the shadings of the geochemical pictures of K2A and for receiving the colors of Fig. 8 and Fig. 13 of K3A is described in Section 3.2 by Walzer and Hendel (1999). Origin and evolution of the geochemical reservoirs of the Earth's silicate spherical shell can be computed by K3A, too. However, in this case, K3A, *we get a more distinct bipartition of mantle*. There is a depleted mantle above and a more primitive mantle below. Walzer and Hendel (1997) made a first somewhat incomplete attempt to model the evolution of the chemical reservoirs of the mantle. Kellog et al. (1999) developed another interesting model for this phenomenon. However, they assumed an intrinsically dense layer in the lower mantle where the density contrast of about 4 % is due to composition alone. This is in contrast to O'Neill and Palme (1998) which gave good reasons why the *gross* chemical composition of the mantle should be uniform, but this uniformity does not apply for incompatible elements and volatiles. Based on geochemical findings of Hofmann (1988) and O'Neill and Palme (1998),

Walzer and Hendel (1999) published a more complete evolution model, more complete in comparison to their 1997 paper. However, the distribution and evolution of the viscosity was taken into account only in a rough manner. The strong influence of the viscosity distribution on the flow pattern in a spherical shell has been shown by Bunge et al. (1997). Therefore, in the present paper we emphasize that it is important to develop a sound viscosity theory and we tried to do so.

We want to stress that our present model has not an integrated lithospheric plate but a continental plate and two oceanic plates which are separated by a low-viscosity spreading zone and subduction zones. So, the plates can run into each other according to the system of governing equations and according to the marginal and initial conditions. The oceanic plates can grow and diminish, the continent can only grow. The mechanism of subduction and spreading is described in Section 2.2 by Walzer and Hendel (1999). This mechanism with small low-viscosity zones in the lithosphere is similar to that by Gurnis (1988). However, in our model the continent is not pinned but it is laterally movable. Furthermore, our continent is not put on the mantle but it develops by chemical differentiation and accretion of free Type 3 tracers to the model continent.

Although we believe that K3A includes relevant features of the mechanism of the thermal and chemical mantle evolution inclusive of spreading and subduction, some features are not present. E.g. in connection with the distribution of deep focus earthquakes, Schmeling et al. (1999) showed that the cold subducting slab may contain metastable olivine below a depth of 410 km. This metastable olivine would be transformed into wadsleyite and ringwoodite, respectively. Schmeling et al. (1999) included the relevant buoyancy effects in their numerical model. Another important feature cannot be included in two-dimensional models: Strongly elongated topographic anomalies have been revealed by satellite altimetry and ship bathymetry which are orthogonal to the mid-ocean ridges. Marquart et al. (1999) explained them by a model of Rayleigh-Taylor instabilities at the lithospheric base.

3.4 Model K3B

K3B is a variant of the model K3 where we neglected the knowledge of the perovskite melting curve according to Zerr and Boehler (1993, 1994) and Boehler (1997). We calculated the viscosity between 771 km depth and the CMB using PREM and eqs (2.12) and (2.13). This is, of course, a decisive disturbance of our model K3A. It is exclusively for lack of space that we present only a few results. Fig. 9 is the counterpart of Fig. 1: Only the viscosity distribution is strongly altered. The first panel of Fig. 9 indicates that, again, the oceanic heat flow, q_{obo} , is greater than the continental heat flow, q_{obc} , for nearly all ages. The laterally averaged heat flow of the total surface of the Earth, q_{ob} , runs somewhat beneath of q_{obo} . The second panel of Fig. 9 shows, likewise, the episodic nature of the generation of the future juvenile continental mass

as a function of time. The lateral continental velocity (third panel) and the vertical mass flow through the 660-km discontinuity (fourth panel of Fig. 9) have an episodic nature and show the appropriate order of magnitude, too. Of course, it is not surprising that the maxima of these curves are situated at different places on the time axis, since the viscosity distribution has been strongly modified.

Fig. 10 depicts four snapshots of the temperature distribution in the mantle, the first of which is for a time in the Archean. Fig. 11 shows four viscosity snapshots. The viscosity values are somewhat lower than in the corresponding panels of Fig. 4. However, the general features are similar to Fig. 4: From top to bottom, we find for all epochs a highly viscous lithosphere, a low-viscosity asthenosphere down to 410 km depth, a high-viscosity transition layer, a low-viscosity zone in the uppermost part of the lower mantle. However, for K3B we have additionally a high viscosity layer near 900 km and a moderate viscosity minimum near 1600 km depth. These features are new. The layer with the highest present-day viscosity of the lower mantle has its maximum near 2600 km depth for K3B, between 2400 and 2500 km depth for K3A. Below it, for both models, the viscosity declines toward the CMB. Fig. 12 shows that, again, the highest lower-mantle maximum of the laterally averaged viscosity rises with declining average mantle temperature. This is in accord with the findings of van den Berg and Yuen (1998). Fig. 13(a) shows an acceleration of the chemical evolution. For K3B, parts of the present-day depleted mantle are also in certain regions of the lower mantle (cf. Fig. 13(b)). But we ought not to forget the fact that also K3B shows a *bipartition* of the mantle with respect to the concentrations of the heat-producing elements, U, Th and K, an evolving continental mass in the appropriate order of magnitude, a lateral continental velocity in the right order of magnitude. The upper mantle is mainly depleted, the lower mantle is mainly rich in incompatible elements, yet, as in the case of K3A. However, for K3A the mentioned bipartition is more pronounced. Finally, we remark that this Section is also a contribution to the variation of parameters (cf. Appendix B).

4 Theory of model S2

The present 3-D spherical-shell model, S2, is based on the numerical solution of the balance equations of momentum, energy and mass in that version given by Walzer et al. (2003 b) where we presented a related model, S1. In comparison to S1 and K3 (cf. Sections 2 and 3), model S2 has the following innovations regarding the assumptions of the model:

a) Based on results of Karato and Lie (1992), Karato and Wu (1993) and Li et al. (1996), we assume a Newtonian rheology in K3, S1 *and* S2, but in S2 we additionally introduce a *viscoplastic yield stress*, σ_y , for the uppermost 285 km. The yielding is defined by an effective viscosity, η_{eff} , where

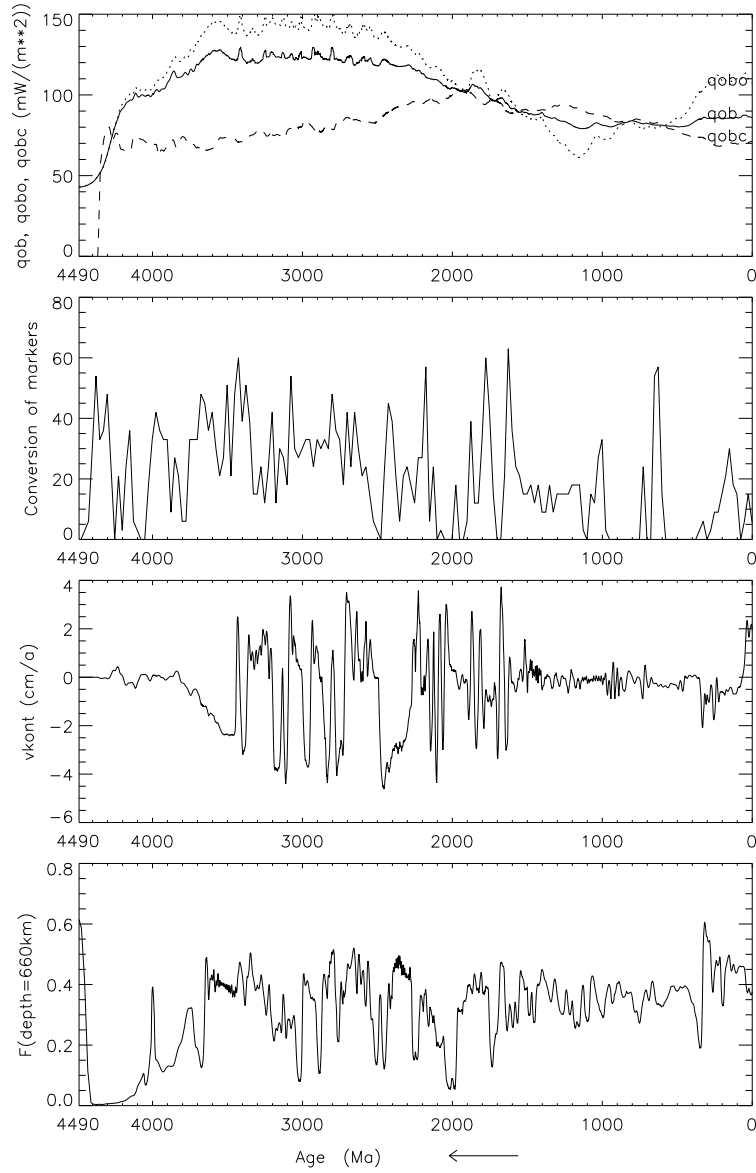


Fig. 9. The evolution of the second new 2-D model of this paper, K3B, presented by some relevant quantities as a function of age. First panel, upper curve: laterally averaged ocean bottom heat flow, q_{obo} . First panel, middle curve: laterally averaged heat flow at the solid surface of the whole Earth, q_{ob} . First panel, lower curve: laterally averaged continental-surface heat flow, q_{obc} . Second panel: number of newly produced Type 3 tracers per 25 Ma. This curve represents the evolution of the juvenile continent material. Third panel: drift velocity of the continent. Fourth panel: vertical mass flow through the 660-km phase boundary.

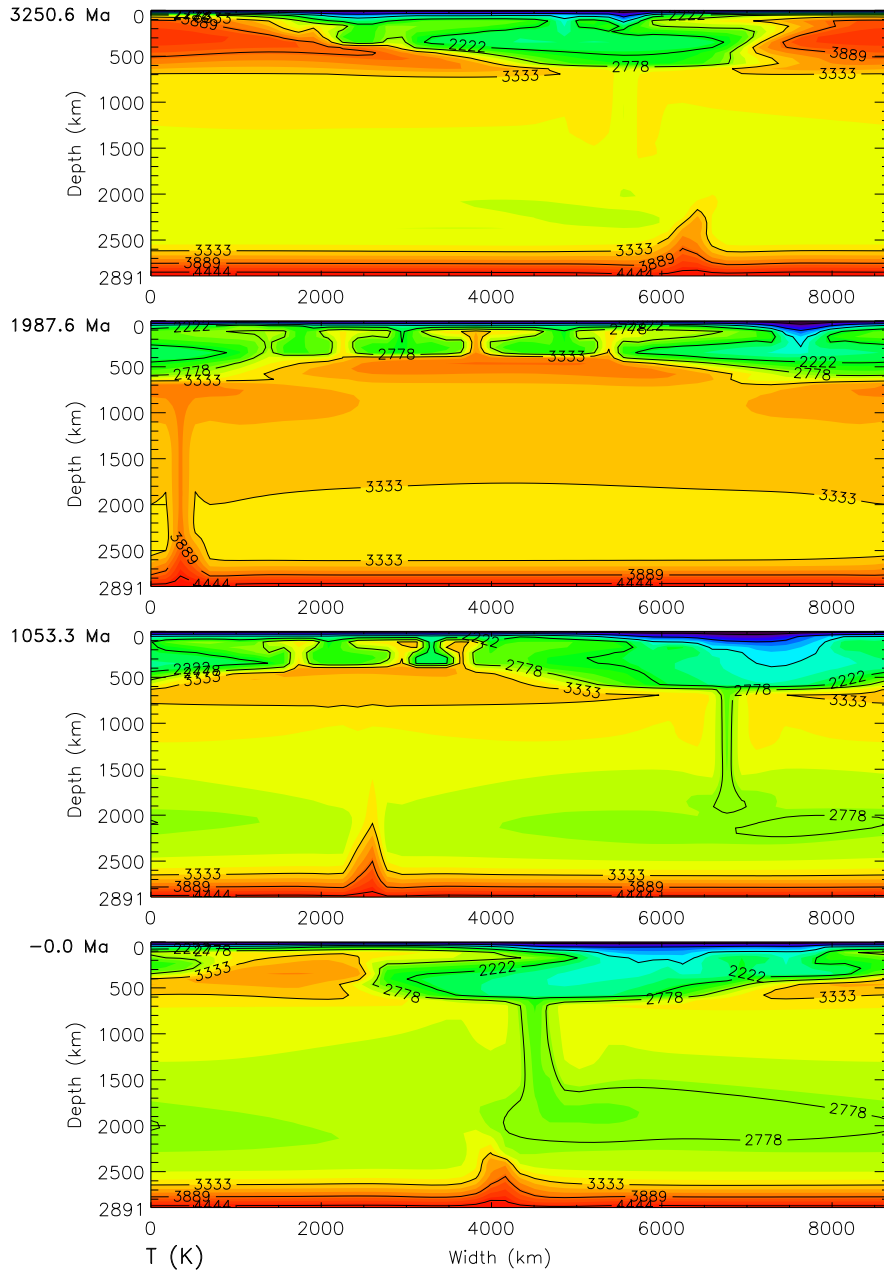


Fig. 10. The temperature, $T(x_1, x_3)$. Model K3B. The ages of the snapshots are given at the upper left corner of each panel.

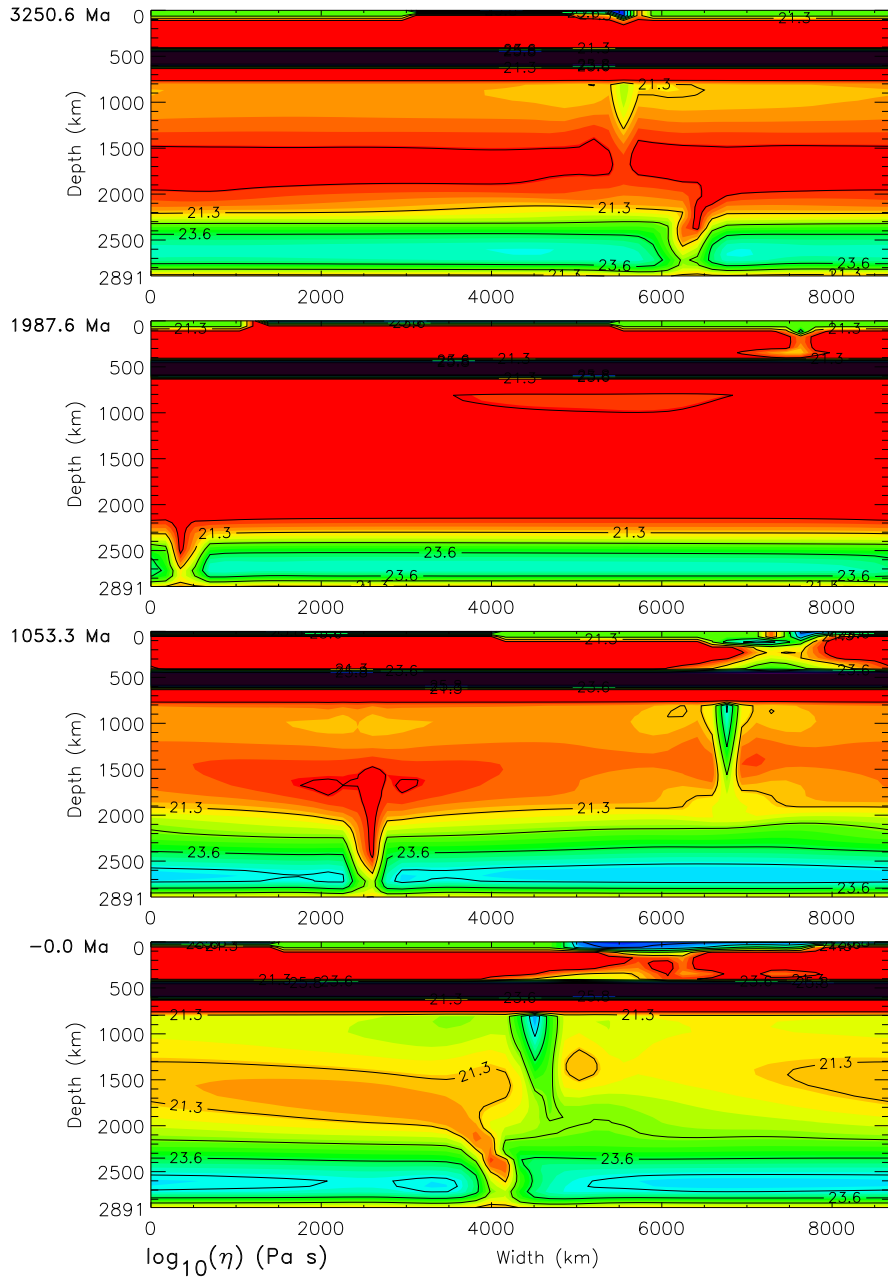


Fig. 11. The evolution of the viscosity of K3B is represented by a series of snapshots. The ages are given at the upper left corner of each panel. The curves are lines of equal logarithm of viscosity in Pa.s.

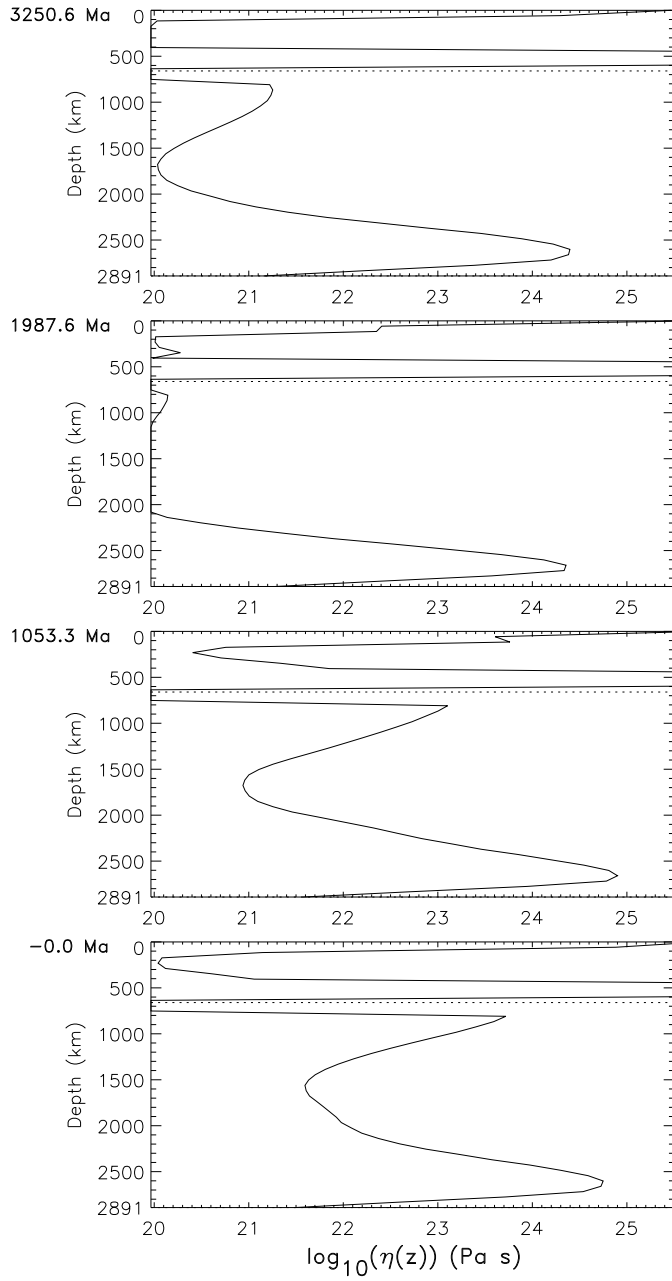


Fig. 12. Four snapshots of K3B. The laterally averaged logarithm of the viscosity is shown as a function of depth. The ages of the snapshots are given at the upper left corner.

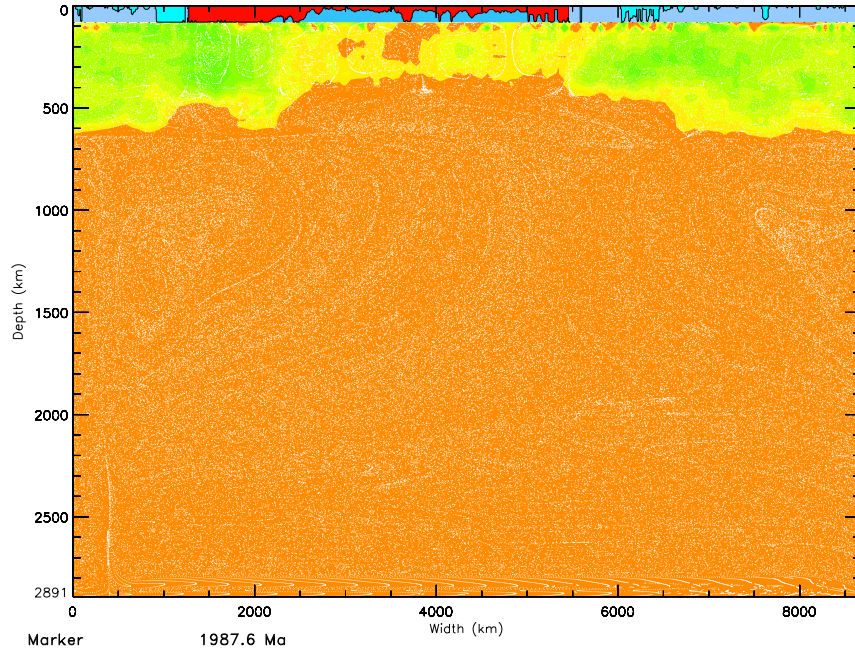


Fig. 13. (a) The evolution of the geochemical reservoirs of K3B. The snapshot is shown for an age of 1987.6 Ma. Orange: a mantle area which is abundant in incompatible elements, yet. Yellow to greenish: depleted to strongly depleted mantle area, virtually the MORB source. Red: continental lithosphere. Light-blue: normal oceanic lithosphere. Dark-blue: oceanic lithosphere with oceanic plateaus.

$$\eta_{eff} = \min \left[\eta(P, T), \frac{\sigma_y}{2\dot{\epsilon}} \right] \quad (4.1)$$

Here, $\dot{\epsilon}$ is the second invariant of the strain-rate tensor, P the pressure and T the temperature.

b) In K3 we used a Cartesian, 2-D, incompressible model with fractionation whereas S1 and S2 are compressible spherical-shell models of thermal convection with homogeneous, exponentially decaying heating from within. The abundances of U, Th and K given by Hofmann (1988) were used in K3 whereas in S1 and S2 the concentrations of U, Th and K in BSE according to McCulloch and Bennett (1994) have been taken into account. We expect that the future structural alterations of S2 toward a compressional, 3-D convection-fractionation model will facilitate the calculation of the balance of the chemical elements. In an incompressible, 2-D, Cartesian mantle model, the balance of U, Th and K is somewhat problematic.

c) In S2 we replaced the Ullmann-Pan'kov equation by the third-order Birch-Murnaghan equation of state

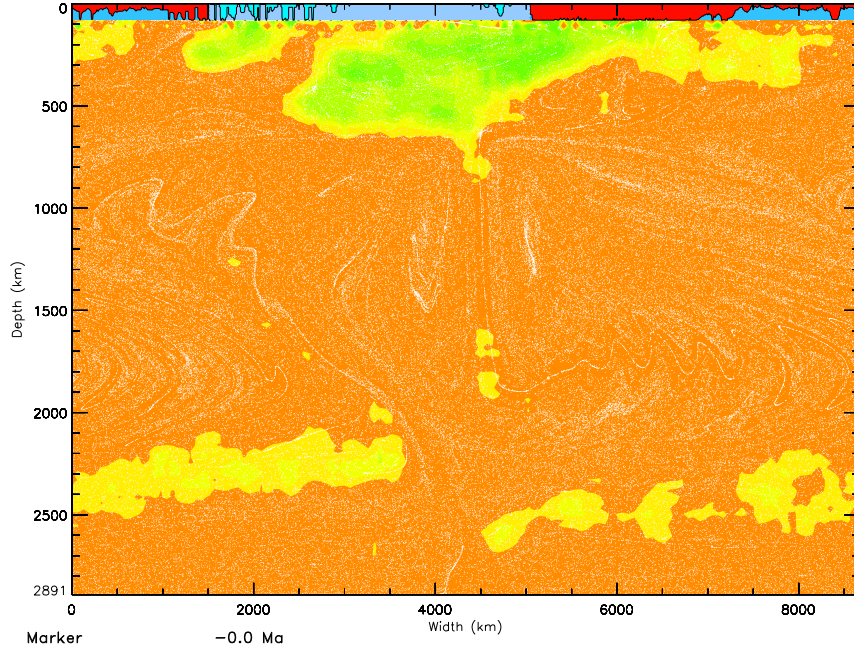


Fig. 13. (b) Text see Fig. 13(a). Here: The snapshot is shown for the geological present.

$$P = \frac{3K_0}{2} \left(x^{-7/3} - x^{-5/3} \right) \left[1 + \frac{3}{4}(K'_0 - 4)(x^{-2/3} - 1) \right] \quad (4.2)$$

where K_0 is the zero-pressure bulk modulus, K'_0 is the pressure derivative of the bulk modulus at vanishing pressure and $x = \rho_0/\rho$ where ρ is the density and ρ_0 a reference density. Using eq (4.2),

$$K = -x(\partial P/\partial x)_T \quad (4.3)$$

and eq (2.9), we derive the Grüneisen parameter, γ , for each layer of the mantle separately from PREM. Inserting the resulting free-volume gamma in Gilvarry's formula

$$\frac{\partial \ln T_m}{\partial \ln x} = 2 \left(\frac{1}{3} - \gamma \right) \left(1 + \gamma c_v \frac{\Delta V}{V} M \right) \quad (4.4)$$

a new melting curve, $T_m(r)$, of the mantle was derived. In eq (4.4), c_v is the specific heat at constant volume, $\Delta V/V$ the relative volume change and M a constant that can be derived from the Debye-Waller formula. The second set of parentheses is nearly unity.

d) For the derivation of the viscosity profile *eta1* of S1, also geochemical considerations were of importance. In this paper, we neglected the corresponding

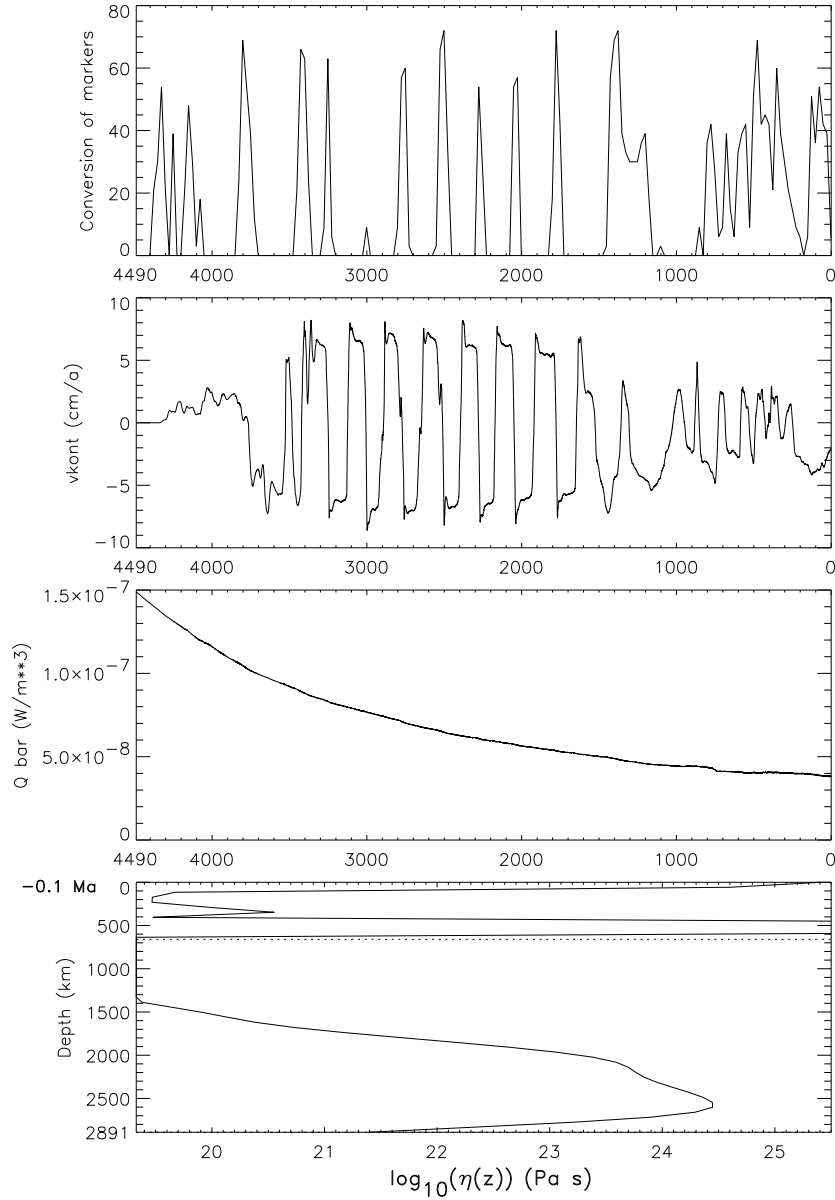


Fig. 14. Results of model K3A. In opposition to the Figs. 1 to 6 and 8 the viscosity factor is here $\eta_{o\lambda} = 2 \times 10^8$ Pa·s. First panel: number of newly produced Type 3 tracers per 25 Ma. This curve represents the evolution of the juvenile continent material. Second panel: drift velocity of the continent. Third panel: the heat production density, averaged over the whole mantle, \bar{Q} . Fourth panel: the laterally averaged logarithm of the viscosity, for the present time, as a function of depth.

ideas and facts during the derivation of the viscosity profile *eta3* of S2 to make the things visible at a glance. Walzer et al. (2003 b) investigated the dynamical consequences of the profile *eta1*. Walzer et al. (2003 a) studied the variation of non-dimensional numbers and its effects on the mechanism of S1. Because of numerical problems, it is not possible to take into account the complete temperature dependence of the viscosity during the solution of the balance equations. Therefore, in the present paper we used the proper number $c=17$ (Karato et al., 2001) for the diffusion creep only in the profile factor $\eta_3(r)$ that appears in the formula

$$\eta(r, \theta, \phi, t) = 10^{r_n} \times \eta_3(r) \times \exp \left[c_t T_m(r) \left(\frac{1}{T(r, \theta, \phi, t)} - \frac{1}{T_{av}(r, t)} \right) \right] \quad (4.5)$$

T_{av} denotes the laterally averaged temperature, r the radius, t the time, θ the colatitude, ϕ the longitude, c_t a constant and r_n a viscosity-level parameter. As a new viscosity profile, *eta3* was derived from PREM, where the Haskell value for 300 km depth was taken as a fixed point. So, the high-viscosity oceanic lithosphere as an upper thermal boundary layer and the low-viscosity D'' layer as a lower thermal boundary layer are already included in $\eta_3(r)$ taking the complete number $c = 17$. In the third factor of the right-hand side of eq (4.5), we supposed only $c_t = 1$ for numerical reasons. So, the lateral variation of the viscosity, η , is too low. But this is not important for the generation of the convective cells since the yield stress, σ_y , is leading for the break-up of the stiff lithosphere anyhow. Fig. 15 presents the laterally averaged viscosity for the end of a typical run, i. e. for the geological present time. Further model parameters are given by Table 5. The density jumps of the two mineral phase transitions are fitted to PREM in order to keep the model consistent. An explanation of the high-viscosity transition layer of Fig. 15 can be found in Karato et al. (1995) who derived a maximum of the viscosity of garnet, but also of the wadsleyite and ringwoodite for the transition zone with a jump at the upper boundary of it to the lower viscosity of the olivine of the asthenosphere and a considerable viscosity jump to the fine-grained perovskite of the uppermost part of the lower mantle. If the creep is diffusion-controlled than a difference in the diffusion coefficient of about 10^3 is to be expected (Karato et al., 1995). Further hints in this direction are given by Weidner et al. (2001). In contrast with the radial viscosity profile *eta1* of S1, the new profile *eta3* and also all laterally averaged viscosities of S2 show a high-viscosity layer exactly at the place of the well-known transition layer and the viscosity gradients at 410 and 660 km depth are very steep. It is now feasible to numerically solve the balance equation with such steep viscosity gradients.

e) In K3 and S1, it was assumed that it does not make sense to keep the temperature at CMB, T_c , constant as a function of colatitude, longitude *and time*, since it is well-known from investigations of komatiites that the temperature of the upper mantle grows less by about 100 K per 10^9 a, that the radioactive heating of the mantle exponentially decays and that already simple parameterized mantle-evolution models show that the Earth is cooling

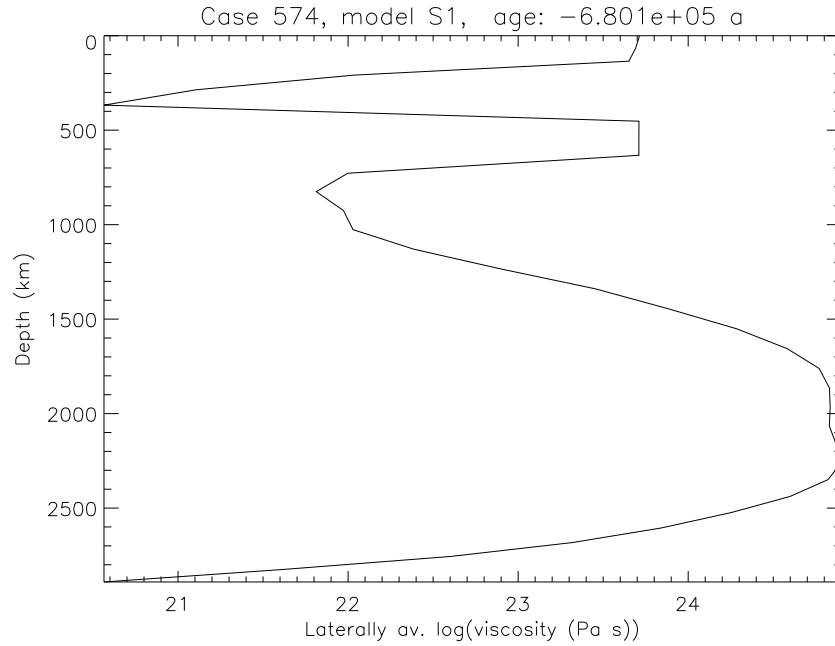


Fig. 15. The laterally averaged viscosity at the end of run 574, i.e. for the geological present time. The profile is mainly determined by *eta3*.

down. Therefore we concluded that it is totally improbable that the laterally averaged CMB temperature, $T_{c,av}$, is constant *with respect to time*. This conclusion applies also for S2. However, we did not take over the thermal CMB boundary condition from S1 to S2. For K3 and S1, it was assumed that the heat flow at CMB, q_c , is constant with respect to time. This assumption was based on parameterized models and considerations by Stevenson et al. (1983), Stacey (1992, Chapter 6.7.5) and Schubert et al. (2001, pp. 607-609). For S2 we abandoned this boundary condition since in this case T_c is not strictly but only approximatively independent of colatitude and longitude. For S2, the *CMB is supposed to be isothermal as a function of the location vector* at a particular time. As other researchers (Steinbach et al., 1993, Steinbach and Yuen, 1994, Honda and Iwase, 1996) have done we adjust the CMB temperature, T_c , after each time step according to the heat flow through the CMB. So, we implemented a simple core-cooling model. In this way, the laterally averaged CMB heat flow as well as the laterally averaged CMB temperature is a function of time.

Table 5. Model parameters

| Parameter | Description | Value | |
|------------------|---|------------------------|--------------------|
| r_{min} | Inner radius of spherical shell | 3.480×10^6 | m |
| r_{max} | Outer radius of spherical shell | 6.371×10^6 | m |
| | Temperature at the outer shell boundary | 288 | K |
| γ_1 | Clapeyron slope for the olivine-spinel transition | $+1.6 \times 10^6$ | Pa K ⁻¹ |
| γ_2 | Clapeyron slope for the spinel-perovskite transition | -2.5×10^6 | Pa K ⁻¹ |
| f_{a1} | Non-dimensional density jump for the olivine-spinel transition | 0.0547 | |
| f_{a2} | Non-dimensional density jump for the spinel-perovskite transition | 0.0848 | |
| | Beginning of the thermal evolution of the Earth's silicate mantle | 4.490×10^9 | a |
| d_1 | Non-dimensional transition width for the olivine-spinel transition | 0.05 | |
| d_2 | Non-dimensional transition width for the spinel-perovskite transition | 0.05 | |
| | Beginning of the radioactive decay | 4.565×10^9 | a |
| c_t | Factor of the lateral viscosity variation | 1 | |
| k | Thermal conductivity | 12 | W/mK |
| $nr + 1$ | Number of radial levels | 33 | |
| | Number of grid points | 1.351746×10^6 | |
| $a_{\mu\nu}(U)$ | Concentration of uranium | 0.0203 | ppm |
| $a_{\mu\nu}(Th)$ | Concentration of thorium | 0.0853 | ppm |
| $a_{\mu\nu}(K)$ | Concentration of potassium | 250 | ppm |

5 Results of Model S2

At first, we present the numerical results of S2 showing our reference run with $r_n = 0$ and $\sigma_y = 1.35 \times 10^8$ Pa. The physical deduction of the viscosity was indeed made for $r_n = 0$. So, r_n has only the task to vary the Rayleigh number, Ra_H . As all other purely viscous models, also S1 (Walzer et al., 2003b) has the result that, for each cell at the surface, the matter flows in different directions from a central point. Compared to other purely viscous models, the improvement of S1 consists in *very* thin cold sheet-like downwellings down to depths of 1200 km and more. In contrast to the surface flow lines of S1, the distribution of the creeping velocity at the surface of the real Earth is totally different: From paleomagnetic investigations on land and on sea, from the age distributions of the volcanic centers in the Hawaiian-Emporer chain, the Tuamotu chain, the MacDonal chain and the Louisville chain (Norton, 2000) and from the distribution of seismic focal plane solutions, it can be concluded that the lithospheric plates of the Earth are piecewise rotating en bloc around

the Earth's center. Each plate has another direction of the angular velocity vector. Fig. 16 shows the surface distributions of the creeping velocities for some younger geological time spans. Substitutionally for lots of runs, Fig. 17 demonstrates that S2 generates planforms with a high-viscosity layer near the surface in a piecewise plate-like, stable motion. Subduction zones and spreading zones have reduced viscosities that are shown in red and yellow colors in Fig. 17. In the case of S2, the convergent and divergent stripe-like surface zones have an Earth-like distribution whereas the convergent subduction zones of S1 are reticularly connected. The subduction zones of the surface can be traced down to the depth. Fig. 18 shows the temperature distribution by colors and creeping velocities by arrows in 632.9 km depth. It is not amazing that the cold sheet-like zones perpendicularly subduct since model S2 does not include chemical differentiation and therefore S2 has no evolving continents. We anticipate that, in a future model, the upper thermal boundary conditions should be differently introduced for continents and oceanic plates. Possibly, the dip angle of the downwelling sheets could be smaller than 90° near the continental margin. The planforms of all runs show that the present model, S2, is nearly a whole-mantle convection model. Therefore, it is no surprise that the resulting S2 geotherms, i.e. $T_{av}(r)$, do not strongly deviate from the geotherms of whole-mantle convection by Schubert et al. (2001).

We calculated the Rayleigh number, Ra_H , by

$$Ra_H = \left\langle \frac{\rho \alpha g h^3}{\kappa \eta_{al}} \cdot \frac{(Qh + q_c)h}{k} \right\rangle \quad (4.6)$$

where α is the thermal expansion coefficient, g gravity acceleration, h depth of the layer. Q is the heat generation rate per unit volume, q_c heat flow at CMB, κ thermal diffusivity, k thermal conductivity. The quantity η_{al} is defined by

$$\log \eta_{al} = \langle \log \eta \rangle \quad (4.7)$$

where the angle brackets stand for the volumetric average but not for a temporal average. Ra_H increases with falling r_n because of eqs (4.5) and (4.6). Fig. 19 summarizes the results of a variation of parameters. The model S2 shows a stable, plate-tectonic behavior for a certain continuous area of moderate values of r_n and σ_y . Furthermore, there are three other planform types which do not reproduce the mentioned features of real mantle convection. A corresponding $Ra_H(2)$ - σ_y plot shows a similar distribution of the planform types but of course standing on its head. $Ra_H(2)$ is the temporal average of Ra_H , averaged over the last 2000 Ma. Walzer et al. (2004) compared the model S2 with newly calculated thermal spherical-shell models using totally different viscosity profiles of other authors, e.g. Kaufmann and Lambeck (2002) and King and Masters (1992). For those models, the calculations revealed only a slight or no tendency to plate-like behavior although we used a similar σ_y range. It is to be presumed that not only the yield stress but also the two interior low-viscosity layers of S2 promote the generation of moving surface

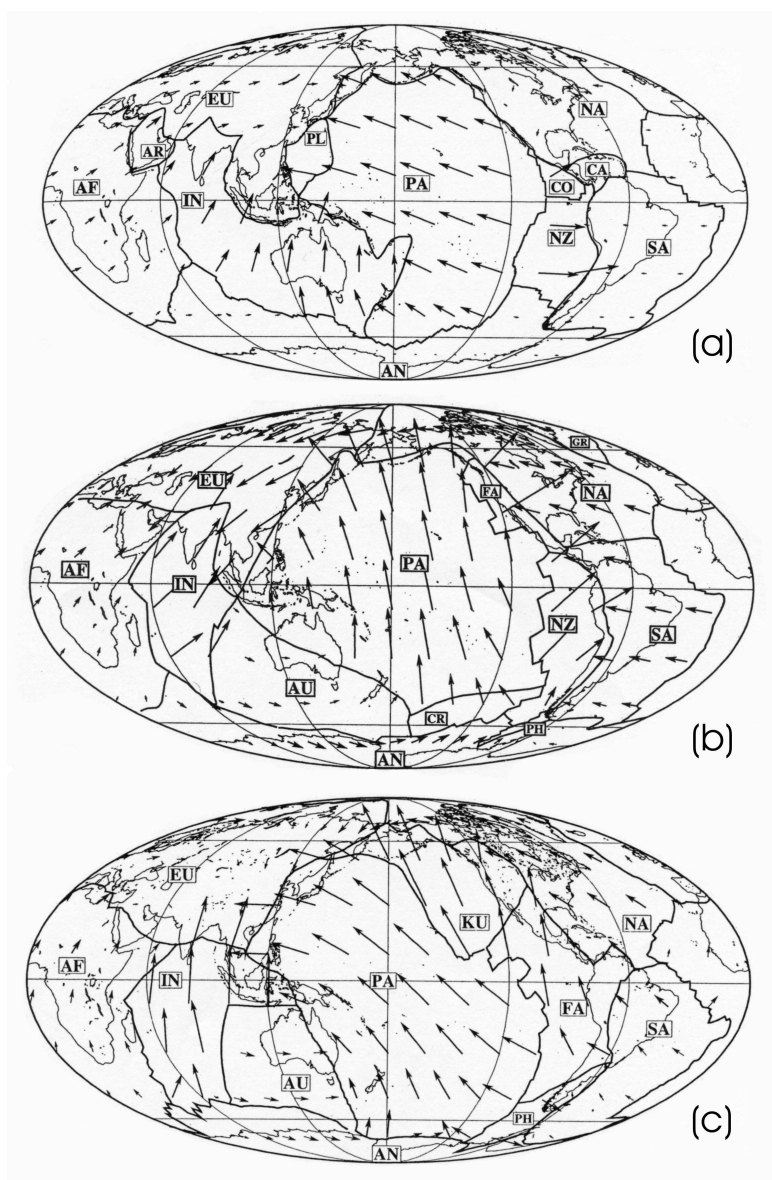


Fig. 16. Observed movements of the oceanic lithospheric plates. The given creeping velocities are relative to the high-viscosity part of the lower mantle. The upper equal-area projection applies for an age of 0 to 10 Ma, the middle projection for 43 to 48 Ma, the lower projection for 74 to 84 Ma. The present position of the continents is maintained for orientation. According to Lithgow-Bertelloni (1998).

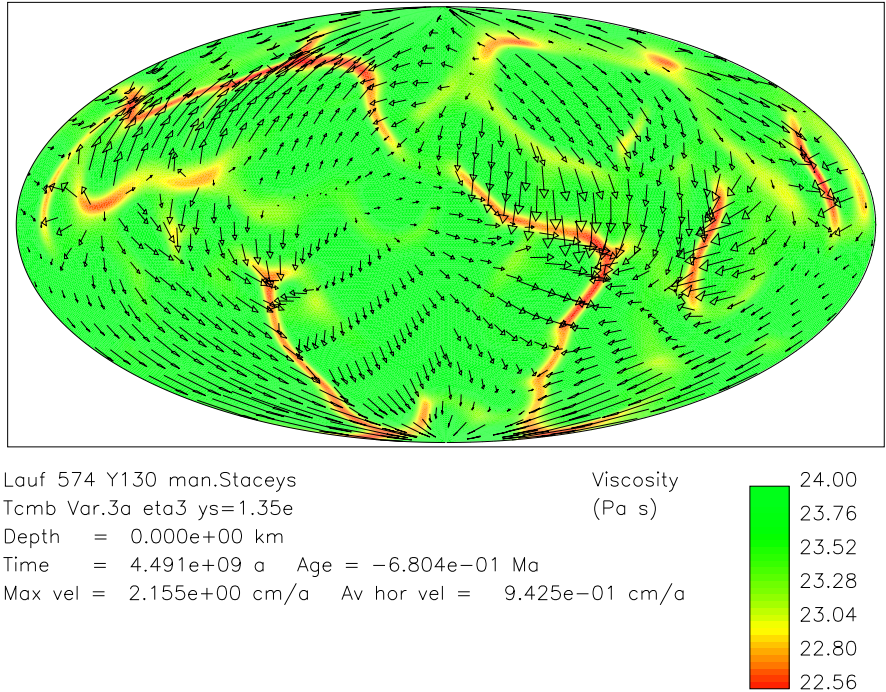


Fig. 17. The surface distribution of log viscosity is given by colors for a viscoplastic yield stress of 135 MPa. The creeping velocities are denoted by arrows. The distribution is plate-like. Red and yellow stripes indicate zones of reduced viscosity due to yielding. The figure stands for the geological present time.

plates. Further results regarding this question can be found in Walzer et al. (2003c).

6 Conclusions

We developed two new models of the evolution of the Earth's mantle. The first model, K3, consists of a 2-D FD Boussinesq convection model with heating from within and from below combined with a simple model of chemical differentiation. Continent and depleted mantle evolve by differentiation of a mantle reservoir which is rich in incompatible elements, yet. In the center of this first part of the paper is the important question: How does the change, over time, of mantle properties (e.g. viscosity and heat production) affect the evolution of the Earth's mantle? There are several main conclusions:

- a) The profile of the laterally averaged viscosity evolves with time and exhibits always a higher viscosity in the transition layer and in the lower part of the lower mantle.

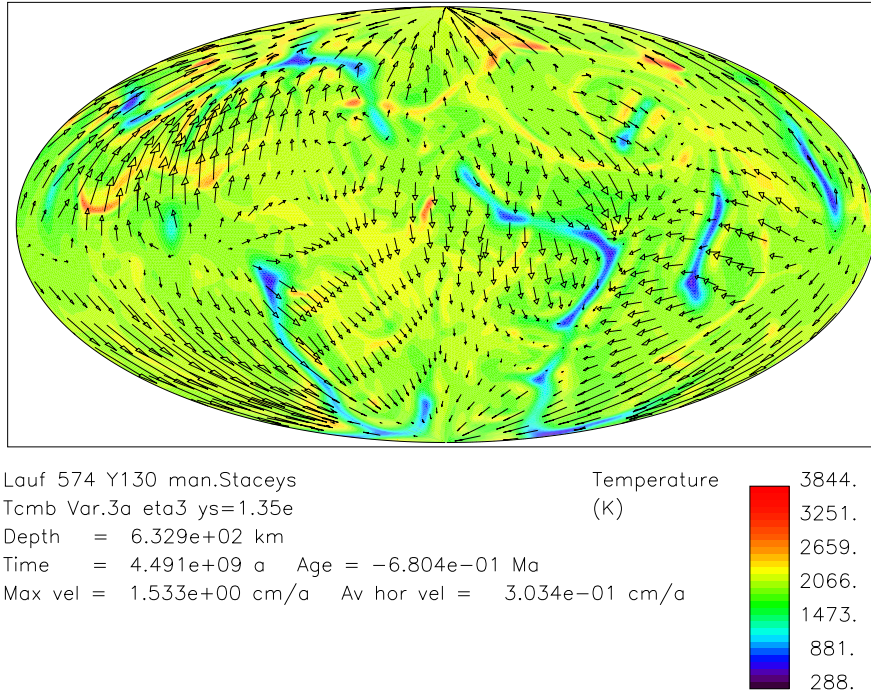


Fig. 18. The temperature distribution (colors) and the creeping velocities (arrows) are shown on an equal-area projection for 632.9 km depth, $\sigma_y = 135$ MPa, $r_n = 0$ and the geological present time. Blue downwelling zones in nearly the same position can be shown for each depth between 0 and 1500 km.

b) Not only the asthenosphere, but also the upper part of the lower mantle is a low-viscosity zone.

c) The high-viscosity transition zone may divide the mantle into two principal reservoirs. It acts as a barrier, but a permeable one, to flow across the mantle transition zone.

d) The chemical differentiation takes place only in the asthenosphere. Therefore, the depleted mantle gathered mainly in the upper mantle.

We obtained a series of reasonable flow-line pictures and the proper order of magnitude of the mantle-creep velocity. It is quite understandable that the highest velocity magnitudes are in the two low-viscosity layers (cf. Fig. 5). Three feed-back mechanisms contributed to the non-steady-state character of the system. One mechanism is generated by the growing inhomogeneity of the heat-source distribution, a second one by the lateral movability of the continent. The third feed-back mechanism is mainly generated by the profile of the laterally averaged viscosity which evolves with time. Each single mechanism is basically simple. The choice of the initial conditions was determined by

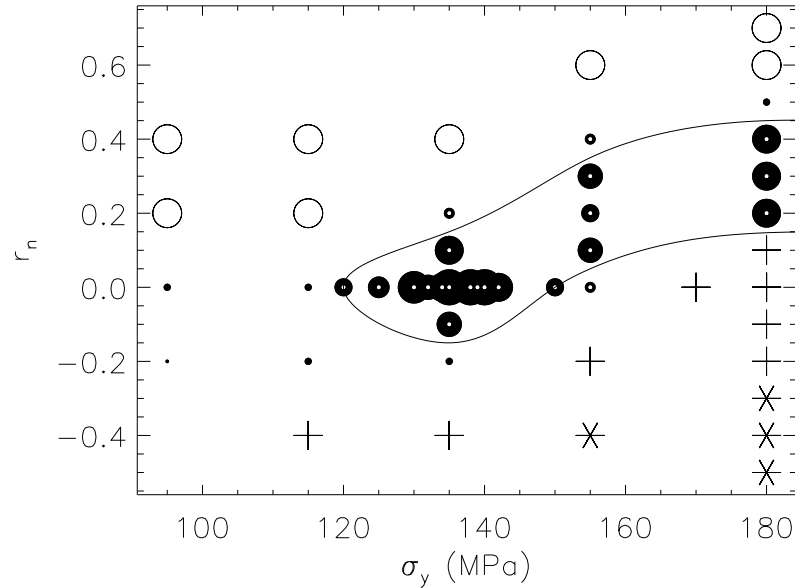


Fig. 19. The distribution of planform types as a function of the viscosity-level parameter, r_n , and the yield stress, σ_y . Little black disks with white center represent runs with plate-like movements near the surface and with thin sheet-like downwellings. White circles stand for runs without surface plates and with a wide-meshed network of broad downwellings. Plus signs denote runs without surface plates that show a diffuse disintegration of the network of cold areas near the surface. Asterisks represent runs without surface plates and without slab-like downwellings as well.

considerations on the cosmogony of the Earth. The relatively high viscosity hill in the lower mantle seems to be the cause for the low lateral movability of the plumes. Contrary to our model K2A, only a few K3A plumes are able to penetrate the transition layer. On the other hand, secondary plumes appear more often in K3A. They are thermically induced in the transition layer. The direct application of seismically derived quantities in order to determine the radius-dependent factor of the viscosity is an essential new feature of this paper.

The second model of this paper, S2, consists of a 3-D FE compressible spherical-shell convection model with a newly derived mantle viscosity profile, called *eta3*, that is deduced from PREM and solid-state physics. Although the profile is related to the viscosity profile of K3, it differs in many details. Also the derivation is different in several respects. There is no chemical fractionation in S2, up to now, but S2 has a homogeneous, exponentially decaying heating from within using the BSE abundances by McCulloch and Bennett (1994). Just this should be the starting point for a future unification of K3

and S2 to form a 3-D FE compressible spherical-shell convection-fractionation model. We hope to be able to simultaneously model not only the growth and the lateral movements of the continents but also the generation of the oceanic plates. Here is the summary of the main results of the present model S2:

A) Based on geophysically observable quantities and on an experimentally derived thermal expansion coefficient as a function of pressure, we derived the Grüneisen parameter, the specific heat at constant pressure, the specific heat at constant volume and the melting temperature, T_m , as a function of radius.

B) Using the findings of A) and results of the Karato group, a new viscosity profile, *eta3*, was derived. We found the following new features: A high-viscosity transition layer with very steep viscosity gradients near the 410-km and 660-km phase transitions lies under the conventional asthenosphere. Now the code can produce stable numerical solutions of the balance equations for the mentioned steep gradients. A second low-viscosity layer beneath the 660 was found. Going deeper, the viscosity gradually rises to a thick, highly viscous central layer of the lower mantle. Also the usual high-viscosity boundary layer on top and the low-viscosity boundary layer above the CMB are included. However, no continental chemical boundary layer is present in S2, up to now.

C) Viscoplastic yield stress and the existence of *two* low-viscosity layers in the interior of the mantle facilitate plate-like behavior near the surface and sheet-like downwellings with an Earth-like distribution.

D) A greater area with stable, plate-like solutions was found by variation of $Ra_H(2)$ and σ_y . There are three other types of planforms out of this area, yet.

E) The temporal evolution of the laterally averaged heat flow at the surface, the Urey number, the Rayleigh number and the kinetic energy of the upper-mantle convection have been computed. They show realistic numerical values. The distribution of the laterally averaged temperature as a function of depth is similar to results of Schubert et al. (2001).

7 Computational aspects

The numerical solutions of the system of balance equations of thermal convection in a compressional spherical shell are obtained using a three-dimensional finite-element discretization, a fast multigrid solver and the second-order Runge-Kutta procedure. The mesh is generated by projection of a regular icosahedron onto a sphere to divide the spherical surface into twenty spherical triangles or ten spherical diamonds. A dyadic mesh refinement procedure connects the midpoints of each side of a triangle with a great circle such that each triangle is subdivided into four smaller triangles. Successive grid refinements generate an almost uniform triangular discretization of the spherical surface of the desired resolution. Corresponding mesh points of spherical surfaces at different depths are connected by radial lines. The radial distribution

of the different spherical-surface networks is so that the volumes of the cells are nearly equal. The details are given by Baumgardner (1983, 1985), Bunge et al. (1997) and Yang (1997). For many runs that we needed for our variation of parameters, we used a mesh with 1351746 nodes. Some runs were made with 10649730 nodes to check the convergence of the lower resolution runs. The result is that the laterally averaged surface heat flow, the Urey number, the Rayleigh number and the Nusselt number as functions of time show hardly any discernable differences ($<0.5\%$). The calculations were performed on 128 processors of a Cray T3E. The code was benchmarked for constant-viscosity convection by Bunge et al. (1997) with numerical results of Glatzmeier (1988) for Nusselt numbers, peak temperatures, and peak velocities. A good agreement ($\leq 1.5\%$) was found.

Acknowledgements

We would like to thank Woo-Sun Yang for his kind help and interesting discussions. Two of us (U.W. and R.H.) gratefully acknowledge the hospitality of Charles Keller, LANL, Los Alamos, NM. This research was supported by the Volkswagenstiftung through the grant I 75474. We thank the Höchstleistungsrechenzentrum Stuttgart and the John von Neumann Institute Jülich for the supply of computing time.

A Appendix: Non-dimensional Variables

Here we introduce non-dimensional variables. They are denoted by primes. The primes have been dropped in eqs (2.16) and (2.17).

| | |
|--|---|
| Heat production density | $Q = Q_0 Q'$ |
| Horizontal component of the location vector | $x_1 = h x'_1$ |
| Vertical component of the location vector | $x_3 = h x'_3$ |
| Density | $\rho = \rho_0 \rho'$ |
| Time | $t = (h^2 / \kappa) t'$ |
| Stream function | $\Psi = \kappa \Psi'$ |
| Temperature | $T = [(Q_0 h + q_{CMB}) h / k] T'$ |
| Horizontal component of the velocity | $v_1 = (\kappa / h) v'_1$ |
| Vertical component of the velocity | $v_3 = (\kappa / h) v'_3$ |
| Pressure | $P = (\kappa \eta_0 / h^2) P' - \rho_0 g h x'_3$ |
| Viscosity | $\eta = \eta_0 \eta'$ |
| Specific heat production | $H = H_0 H'$ |
| Specific isotopic heat production 4.55 × 10 ⁹ years ago | $H_{0\nu} = H_0 H'_{0\nu}$ |
| Magnitude of the heat flow | $q = (Q_0 h + q_{CMB}) q'$ |
| Clapeyron slope of the <i>k</i> th phase transition | $\gamma_k = [\rho_0 g k / (Q_0 h + q_{CMB})] \gamma'_k$ |

B Appendix: Variation of the parameters of K3A and K3B

The Figs. 1 to 8 show that a certain amount of geophysical quantities and fields with Earth-like orders of magnitude are the consequence of model K3A with a set of fixed Earth-like parameters. We received the laterally averaged surface heat flow densities for the total surface, for the ocean and for the continent, the juvenile continental growth, the lateral drift velocity of the continent v_{cont} , the vertical mass flow through the 660-km discontinuity, the heat production rate averaged over the whole mantle, and the Nusselt number. The mentioned quantities are plotted as functions of age. Moreover, the temperature field, the viscosity field, the laterally averaged logarithm of viscosity, the field of incompatible elements and other fields have been calculated for some characteristic moments. All model assumptions are published and, nevertheless, the structure of model K3A is not very complex. So, it is thoroughly non-trivial to receive the mentioned set of quantities with acceptable orders of magnitude. A variation of the input parameters showed that the alteration of the viscosity factor $\eta_{o\lambda}$ had the strongest influence on the results. If we vary $\eta_{o\lambda}$ between 3.6×10^8 and 4.4×10^8 Pa · s using small steps, nevertheless, the curves of continental growth, the lateral drift velocity of the continent as a function of time and the laterally averaged viscosity as a function of depth and of time, do not alter their characteristic features. The Figs. 1 to 6 as well as 8 represent the results for $\eta_{o\lambda} = 4.0 \times 10^8$ Pa · s. Also the total continental mass and the percentage of the depleted mantle stay in the right order of magnitude for the mentioned variation of the viscosity factor $\eta_{o\lambda}$. The Nusselt number versus $\eta_{o\lambda}$ plot shows only a very flat curve nearly parallel to the $\eta_{o\lambda}$ axis for the mentioned $\eta_{o\lambda}$ interval. The Earth-like character of the results *gradually* vanishes out of this interval, e.g., Fig. 14 shows some results of K3A for $\eta_{o\lambda} = 2 \times 10^8$ Pa · s. The first panel demonstrates that the episodic character of the growth of juvenile continental material continues to exist. The lateral velocity of the continent is plotted as a function of age in the second panel. In the central part of the modelled Earth's history, it is nearly periodic. It is also in the right order of magnitude. The time dependence of the heat production rate, averaged over the whole volume, and the present-day curve of the laterally averaged logarithm of the viscosity as a function of depth are very similar to the results of K3A for $\eta_{o\lambda} = 4 \times 10^8$ Pa · s (cf. third and fourth panels of Fig.14). The introduction of model K3B (see Section 3.4) causes a more drastic variation of the parameters, yet. We varied also the initial temperature curve and made some runs with starting temperatures between $0.8 T_{init}$ and $1.0 T_{init}$. The results were very similar, only the amount of evolved continental mass was lower, because of the mechanism of chemical differentiation.

C Appendix: Thermodynamics and the Ullmann-Pan'kov equation of state

This Appendix serves as a concise deduction of the Eqs. (2.1) and (2.2). At first only equilibrium thermodynamics is used. The quantity x is the volume ratio

$$x = V/V_0 = \rho_0/\rho \quad (\text{C1})$$

where ρ_0 is the density at zero pressure and at a reference temperature T_0 ; ρ is the density, V is a volume with a special mass at pressure P and at temperature T ; the same mass occupies a volume V_0 at zero pressure and at T_0 . In equilibrium the differential of the Helmholtz free energy, F , is

$$dF = -SdT - PdV = -SdT - V_0Pdx \quad (\text{C2})$$

where S denotes the entropy. Hence, it follows that

$$V_0P = -\left(\frac{\partial F}{\partial x}\right)_T \quad (\text{C3})$$

for an isothermal surrounding. If the internal energy is denoted E , then from

$$dE = TdS - PdV \quad (\text{C4})$$

it follows that

$$V_0P = -\left(\frac{\partial E}{\partial x}\right)_S \quad (\text{C5})$$

for a surrounding with constant entropy. If we treat the adiabatic case then

$$E = V_0U(x, S) \quad (\text{C6})$$

For the isothermal case

$$F = V_0U(x, T) \quad (\text{C7})$$

applies. Generalized we have

$$U = U(x, \xi) \quad (\text{C8})$$

where ξ can be S or T . Hence

$$P = -(\partial U/\partial x)_\xi \quad (\text{C9})$$

The bulk moduli are defined by

$$K_\xi = -V\left(\frac{\partial P}{\partial V}\right)_\xi \quad (\text{C10})$$

From eqs (C1), (C9) and (C10) it follows that

$$K_\xi = x \left(\frac{\partial^2 U}{\partial x^2} \right)_\xi \quad (\text{C11})$$

From eqs (C1), (C10) and (C11)

$$-\frac{K_\xi}{x} = \left(\frac{\partial P}{\partial x} \right)_\xi = - \left(\frac{\partial^2 U}{\partial x^2} \right)_\xi \quad (\text{C12})$$

If we differentiate eq (C11) then we receive

$$\left(\frac{\partial K_\xi}{\partial x} \right)_\xi = \left(\frac{\partial^2 U}{\partial x^2} \right)_\xi + x \left(\frac{\partial^3 U}{\partial x^3} \right)_\xi \quad (\text{C13})$$

Inserting eq (C13) and diving by eq (C12) we get

$$\left(\frac{\partial K_\xi}{\partial P} \right)_\xi = \left(\frac{\partial K_\xi}{\partial x} \right)_\xi / \left(\frac{\partial P}{\partial x} \right)_\xi = -1 - \frac{x^2}{K_\xi} \left(\frac{\partial^3 U}{\partial x^3} \right)_\xi = -\frac{x}{K_\xi} \left(\frac{\partial K_\xi}{\partial x} \right)_\xi \quad (\text{C14})$$

The independent variable of U , x , can be replaced by differing auxiliary variables, y , e.g. by

$$y = \frac{3}{2}(1 - x^{-2/3}) \quad (\text{C15})$$

This expression results from the Almansi-Hamel tensor of order two and the Euler variables. Using it we get the second-order Birch-Murnaghan equation of state (EoS). In this case, y is the infinitesimal strain. Ullmann and Pan'kov (1976) proposed

$$y = u_1^{-1}(x^{u_1} - 1) \quad (\text{C16})$$

in place of eq (C15). The quantity u_1 means

$$u_1 = (2 - K'_0)/3 \quad (\text{C17})$$

Using eq (C16), the series development of U has a favourable convergence. Furthermore, for $K'_0 = 4$ the second-order Birch-Murnaghan EoS proved to be a particular case of the Ullmann-Pan'kov EoS (see also Anderson, 1995). As usual, K'_0 stands for the pressure derivative of the bulk modulus at vanishing pressure. Ullmann and Pan'kov (1976) proceeded as follows where the strongly condensed description stems from us: If the volume ratio, x , is replaced by the auxiliary quantity, y , then Y is defined by

$$U = Y(y, \xi) \quad (\text{C18})$$

The quantity y must vanish for $x = 1$. Apart from that, there is a such monotonous dependence between x and y that $\partial Y(0, \xi)/\partial y$ vanishes. From eq (C11) it follows that both bulk moduli at zero pressure can be expressed by

$$K_0 = \partial^2 Y(0, \xi)/\partial y^2 \quad (\text{C19})$$

where the index ξ at K_0 has been omitted. Note that $x = 1$ at $y = 0$. It is possible to deduce a multitude of known and new equations of state from a multitude of formulae $y = y(x)$. It is usual to develop these equations of state into a Taylor series and to truncate after a certain term according to the requested accuracy. Here, we receive

$$U = \frac{1}{2}K_0y^2 \left[1 + 2 \sum_{n=1}^N Y_{n+2} \frac{y^n}{(n+2)!} \right] + \frac{\partial^{N+3}Y(\vartheta_N y, \xi)}{\partial y^{N+3}} \cdot \frac{y^{N+3}}{(N+3)!} \quad (\text{C20})$$

where the auxiliary quantities Y_{n+2} are defined by

$$Y_{N+2} = K_0^{-1} \frac{\partial^{n+2}Y(0, \xi)}{\partial y^{n+2}} \quad (\text{C21})$$

ϑ_N is an unknown function of y and N . Its values are between 0 and 1. Starting from the general relation

$$y = y(x, \xi) \quad (\text{C22})$$

the n -th derivative of U with respect to x can be represented as follows (cf. Ryshik and Gradstein, 1957)

$$\frac{\partial^n U}{\partial x^n} = \sum_{m=1}^n F_{n,m} \frac{\partial^m Y}{\partial y^m} \quad (\text{C23})$$

A special case is

$$\frac{\partial^3 U}{\partial x^3} = F_{3,1} \frac{\partial Y}{\partial y} + F_{3,2} \frac{\partial^2 Y}{\partial y^2} + F_{3,3} \frac{\partial^3 Y}{\partial y^3} \quad (\text{C24})$$

where

$$F_{n,1} = \frac{\partial^n y}{\partial x^n} \quad \text{and} \quad F_{n,n} = \left(\frac{\partial y}{\partial x} \right)^n \quad (\text{C25})$$

as well as

$$F_{n+2,2} = \sum_{k=1}^{\lfloor \frac{n+2}{2} \rfloor} l_k \binom{n+2}{k} \frac{\partial^k y}{\partial x^k} \frac{\partial^{n+2-k} y}{\partial x^{n+2-k}} \quad (\text{C26})$$

The quantity $\lfloor \frac{n+2}{2} \rfloor$ is the greatest integer not greater than $\frac{n+2}{2}$, whereas l_k is 1 or $\frac{1}{2}$ for $k \leq \frac{n+2}{2}$, respectively. Inserting eq (C24) in eq (C14) and using eqs (C25) and (C26) we arrive at

$$\begin{aligned} \left(\frac{\partial K_\xi}{\partial P} \right)_\xi = & -1 - 3x \left(\frac{\partial y}{\partial x} \right)^{-1} \frac{\partial^2 y}{\partial x^2} - \frac{x^2}{K_\xi} \left(\frac{\partial y}{\partial x} \right)^3 \frac{\partial^3 Y}{\partial y^3} - \frac{P}{K_\xi} x^2 \left(\frac{\partial y}{\partial x} \right)^{-2} \times \\ & \times \left[3 \left(\frac{\partial^2 y}{\partial x^2} \right)^2 - \frac{\partial y}{\partial x} \frac{\partial^3 y}{\partial x^3} \right] \end{aligned} \quad (\text{C27})$$

This relation applies for each EoS for which an equation $y(x)$ with the foregoing conditions is defined. From the general eq (C27), eq (2.1) can be deduced assuming especially the eqs (C16) and (C17). In this case, the third term of the right-hand side of eq (C27) has been considered as neglectable. Taking into account the vanishing of some middle terms of the right-hand side of eq (C20) in the case of assumption (C16), the relation

$$U = \frac{K_0}{2u_1^2}(x^{u_1} - 1)^2 \left[1 + \frac{Y_4}{12u_1^2}(x^{u_1} - 1)^2 \right] \quad (C28)$$

is derivable from eq (C20) where also the derivatives of eq (C16) must be inserted in eq (C20), namely

$$\partial y / \partial x = x^{u_1-1} \quad (C29)$$

$$\partial^2 y / \partial x^2 = (u_1 - 1)x^{u_1-2} \quad (C30)$$

$$\partial^3 y / \partial x^3 = (u_1 - 1)(u_1 - 2)x^{u_1-3} \quad (C31)$$

Y_4 is deduced from eq (C21). Using eqs (C17) and (C31) we receive a relatively small remainder term for the Ullmann-Pan'kov equation

$$Y_4 = \frac{1}{9}(1 + K'_0)(2K'_0 - 1) + K_0K''_0 \quad (C32)$$

where K''_0 is the second derivative of the bulk modulus at zero pressure. Anderson (1995) deals with the problem with truncation of series. He compares the remainder term of the Birch-Murnaghan EoS, of the Thomsen EoS and of the Bardeen EoS with eq (C32). For $Y_4 \approx 0$, eq (2.2) follows from eqs (C17) and (C28).

References

1. Abbott, D.A., Drury, R., Mooney, W.D., 1997. Continents as lithological icebergs: the importance of buoyant lithospheric roots. *Earth Planet. Sci. Lett.*, 149, 15-27.
2. Anderson, O.L., 1995. *Equations of State of Solids for Geophysics and Ceramic Science*. Oxford University Press, New York, Oxford.
3. Armstrong, R.L., 1968. A model for the evolution of strontium and lead isotopes in a dynamic Earth. *Rev. Geophys.*, 6, 175- 199.
4. Armstrong, R.L., 1991. The persistent myth of crustal growth. *Australian J. Earth Sci.*, 38, 613-640.
5. Baumgardner, J.R., 1983. A three-dimensional finite element model for mantle convection. Thesis, Univ. of California, Los Angeles.
6. Baumgardner, J.R., 1985. Three-dimensional treatment of convective flow in the Earth's mantle. *J. Stat. Phys.* 39 (5-6), 501-511.
7. Bercovici, D., Karato, S.-I., 2003. Whole-mantle convection and the transition-zone water filter. *Nature* 425, 39-44.

8. Boehler, R., 1997. The temperature in the Earth's core. In: Crossley, D.J. (Ed.), *Earth's Deep Interior*. Gordon Breach Sci. Publ., Amsterdam. pp. 51-63.
9. Bunge, H.-P., Richards, M.A., Baumgardner, J.R., 1997. A sensitivity study of three-dimensional spherical mantle convection at 10^8 Rayleigh number: effects of depth-dependent viscosity, heating mode, and an endothermic phase change. *J. Geophys. Res.*, 102, 11991-12007.
10. Čadež, O., van den Berg, A.P., 1998. Radial profiles of temperature and viscosity in the Earth's mantle inferred from the geoid and lateral seismic structures. *Earth Planet. Sci. Lett.*, 164, 607-615.
11. Christensen, U.R., Yuen, D.A., 1985. Layered convection induced by phase transitions. *J. Geophys. Res.*, 90, 10291-10300.
12. Clayton, R.N., Mayeda, T.K., 1996. Oxygen isotope composition of achondrites. *Geochem. Cosmochem. Acta*, 60, 1999-2017.
13. Condie, K.C., 1998. Episodic continental growth and supercontinents: a mantle avalanche connection?. *Earth Planet. Sci. Lett.*, 163, 97-108.
14. Cserepes, L., Yuen, D.A., 1997. Dynamical consequences of mid-mantle viscosity stratification on mantle flows with an endothermic phase transition. *Geophys. Res. Lett.*, 24, 181-184.
15. Dalrymple, G.B., 1991. *The Age of the Earth*. Stanford University Press, Stanford.
16. Doin, M.-P., Fleitout, L., Christensen, U., 1997. Mantle convection and stability of depleted and undepleted continental lithosphere. *J. Geophys. Res.*, 102, No. B2, 2771-2787.
17. Drury, M.R., Fitz Gerald, J.D., 1998. Mantle rheology: insights from laboratory studies of deformation and phase transition. In: Jackson, I. (Ed.), *The Earth's Mantle*. Cambridge Univ. Press, Cambridge. pp. 503-559.
18. Dziewonski, A.M., Anderson, D.L., 1981. Preliminary reference Earth model. *Phys. Earth Planet. Int.*, 25, 297-356.
19. Frost, H.J., Ashby, M.F., 1982. *Deformation Mechanism Maps: The Plasticity and Creep of Metals and Ceramics*. Pergamon Press, Oxford.
20. Gilvarry, J.J., 1956. The Lindemann and Grüneisen Laws. *Phys. Rev.* 102, 307-317.
21. Glatzmaier, G.A., 1988. Numerical simulations of mantle convection: time-dependent, three-dimensional, compressible, spherical shell. *Geophys. Astrophys. Fluid Dyn.* 43, 223-264.
22. Gurnis, M., 1988. Large-scale mantle convection and the aggregation and dispersal of supercontinents. *Nature*, 332, 695-699.
23. Hayashi, C., Nakazawa, K., Nakagawa, Y., 1985. Formation of the solar system. In: Black, D.C., Matthews, M.S. (Eds.), *Protostars and Planets II*. University of Arizona Press, Tucson.
24. Hofmann, A.W., 1988. Chemical differentiation of the Earth: the relationship between mantle, continental crust, and oceanic crust. *Earth Planet. Sci. Lett.*, 90, 297-314.
25. Hofmann, A.W., 1997. Mantle chemistry: the message from oceanic volcanism. *Nature*, 385, 219-229.
26. Honda, S., Iwase, Y., 1996. Comparison of the dynamic and parameterized models of mantle convection including core cooling. *Earth Planet. Sci. Lett.* 139, 133-145.

27. Irvine, R.D., Stacey, F.D., 1975. Pressure dependence of the thermal Grüneisen parameter, with application to the Earth's lower mantle and outer core. *Phys. Earth Planet. Int.*, 11, 157-165.
28. Ito, E., Matsui, Y., 1978. Synthesis and crystal-chemical characterization of MgSiO_3 perovskite. *Earth Planet. Sci. Lett.*, 38, 443-450.
29. Karato, S., 1989. Defects and plastic deformation of olivine. In: Karato, S., Toriumi, M. (Eds.), *Rheology of Solids and of the Earth*. Oxford Univ. Press, Oxford. pp. 176-208.
30. Karato, S., 1997. Phase transformations and rheological properties of mantle minerals. In: Crossley, D.J. (Ed.), *Earth's Deep Interior*. Gordon Breach Sci. Publ., Amsterdam. pp. 223-272.
31. Karato, S., Li, P., 1992. Diffusion creep in perovskite: implications for the rheology of the lower mantle. *Science*, 255, 1238-1240.
32. Karato, S., Wu, P., 1993. Rheology of the upper mantle: a synthesis. *Science*, 260, 771-778.
33. Karato, S., Wang, Z., Liu, B., Fujino, K., 1995. Plastic deformation of garnets: systematics and implications for the rheology of the mantle transition zone. *Earth Planet. Sci. Lett.*, 130, 13-30.
34. Kaufmann, G., Lambeck, K., 2002. Glacial isostatic adjustment and the radial viscosity profile from inverse modeling. *J. Geophys. Res.* 107 (B11), 2280 (doi: 10.1029/2001JB000941).
35. Kellogg, L.H., Hager, B.H., van der Hilst, R.D., 1999. Compositional stratification in the deep mantle. *Science*, 283, 1881-1884.
36. Kido, M., Čadek, O., 1997. Inferences of viscosity from the oceanic geoid: indication of a low viscosity zone below the 660-km discontinuity. *Earth Planet. Sci. Lett.*, 151, 125-137.
37. Kido, M., Yuen, D.A., Čadek, O., Nakakuki, T., 1998. Mantle viscosity derived by genetic algorithms using oceanic geoid and seismic tomography for whole-mantle versus blocked-flow situations. *Phys. Earth Planet. Int.*, 107, 307-326.
38. King, S.D., Masters, G., 1992. An inversion for radial viscosity structure using seismic tomography. *Geophys. Res. Lett.*, 19, 1551-1554.
39. Leibfried, G., Ludwig, W., 1961. Theory of anharmonic effects in crystals. *Solid State Phys.*, 12, 275-444.
40. Li, P., Karato, S., Wang, Z., 1996. High-temperature creep in fine-grained polycrystalline CaTiO_3 , an analogue material of $(\text{Mg,Fe})\text{SiO}_3$ perovskite. *Phys. Earth Planet. Int.*, 95, 19-36.
41. Lister, J.R., Buffett, B.A., 1995. The strength and efficiency of thermal and compositional convection in the geodynamo. *Phys. Earth Planet. Int.*, 91, 17-30.
42. Lithgow-Bertelloni, C., Richards, M.A., 1998. The dynamics of Cenozoic and Mesozoic plate motions. *Rev. Geophysics* 36, 27-78.
43. Marquart, G., Schmeling, H., Braun, A., 1999. Small-scale instabilities below the cooling oceanic lithosphere. *Geophys. J. Int.*, 138, 655-666.
44. McCulloch, M.T., Bennett, V.C., 1994. Progressive growth of the Earth's continental crust and depleted mantle geochemical constraints. *Geochim. Cosmochim. Acta*, 58, 4717-4738.
45. McCulloch, M.T., Bennett, V.C., 1998. Early differentiation of the Earth: an isotopic perspective. In: Jackson, I. (Ed.), *The Earth's Mantle*. Cambridge Univ. Press, Cambridge. pp. 127-158.

46. Nellis, W.J., 2000. Metallization of fluid hydrogen at 140Gpa (1.4Mbar): implications for Jupiter. *Planetary and Space Science*, 48, 671-677.
47. Norton, I.O., 2000. Global hot spot reference frames and plate motion. In: Richards, M.A., Gordon, R.G., van der Hilst, R.D., (Eds.), *The History and Dynamics of Global Plate Motions*. AGU, Washington, DC, pp. 339-357.
48. Nutman, A.P., McGregor, V.R., Friend, C.R.L., Bennett, V.C., Kinny, P.D., 1996. The Itsaq gneiss complex of southern West Greenland; the world's most extensive record of early crustal evolution (3900-3600 Ma). *Precambrian Research*, 78, 1-39.
49. O'Neill, H.S.C., Palme, H., 1998. Composition of the silicate Earth: implications for accretion and core formation. In: Jackson, I. (Ed.), *The Earth's Mantle*. Cambridge Univ. Press, Cambridge. pp. 3-126.
50. Ohtani, E., 1983. Melting temperature distribution and fractionation in the mantle. *Phys. Earth Planet. Int.*, 33, 12-25.
51. Pari, G., Peltier, W.R., 1998. Global surface heat flux anomalies from seismic tomography-based models of mantle flow: implications for mantle convection. *J. Geophys. Res.*, 103, 23743-23780.
52. Poirier, J.P., 1988. Lindemann law and the melting temperature of perovskites. *Phys. Rev. Lett.*, 54, 364-369.
53. Poirier, J.P., 1991. *Introduction to the Physics of the Earth's Interior*. Cambridge University Press, Cambridge etc.
54. Pollack, H.N., Hurter, S.J., Johnson, J.R., 1993. Heat flow from the Earth's interior: analysis of the global data set. *Rev. Geophys.*, 31, 267-280.
55. Ranalli, G., 1998. Inferences on mantle rheology from creep laws. *GeoResearch Forum*, 3-4, 323-340.
56. Richter, F.M., 1973. Finite amplitude convection through a phase boundary. *Geophys. J. R. Astron. Soc.*, 35, 265-276.
57. Ringwood, A.E., 1990. Slab-mantle interactions: petrogenesis of intraplate magmas and structure of the upper mantle. *Chem. Geol.*, 82, 187-207.
58. Ringwood, A.E., 1991. Phase transformations and their bearing on the constitution and dynamics of the mantle. *Geochim. Cosmochim. Acta*, 55, 2083-2110.
59. Rudnick, R., 1995. Making continental crust. *Nature*, 378, 571-577.
60. Ryshik, I.M., Gradstein, I.S., 1957. *Summen-, Produkt- und Integraltafeln*. Deutscher Verlag der Wissenschaften, Berlin.
61. Schmeling, H., Monz, R., Rubie, D.C., 1999. The influence of olivine metastability on the dynamics of subduction. *Earth Planet. Sci. Lett.*, 165, 55-66.
62. Schubert, G., Turcotte, D.L., Olson, P., 2001. *Mantle Convection in the Earth and Planets*. Cambridge Univ. Press, Cambridge, etc., 940 pp.
63. Sleep, N.H., 1990. Hot spots and mantle plumes: some phenomenology. *J. Geophys. Res.*, 95, 6715-6736.
64. Stacey, F.D., 1992. *Physics of the Earth*. p. 459, Brookfield Press, Brisbane.
65. Stacey, F.D., Irvine, R.D., 1977a. Theory of melting: thermodynamic basis of Lindemann's law. *Austral. J. Phys.*, 30, 631-640.
66. Stacey, F.D., Irvine, R.D., 1977b. A simple dislocation theory of melting. *Austral. J. Phys.*, 30, 641-646.

67. Steinbach, V., Yuen, D.A., 1992. The effects of multiple phase transitions on Venusian mantle convection. *Geophys. Res. Lett.*, 19, 2243-2246.
68. Steinbach, V., Yuen, D.A., 1994. Effects of depth-dependent properties on the thermal anomalies produced in flush instabilities from phase transitions. *Phys. Earth Planet. Inter.* 86, 165-183.
69. Steinbach, V., Yuen, D.A., Zhao, W.L., 1993. Instabilities from phase transitions and the timescales of mantle thermal evolution. *Geophys. Res. Lett.* 20, 1119 - 1122.
70. Stevenson, D.J., Spohn, T., Schubert, G., 1983. Magnetism and thermal evolution of the terrestrial planets. *Icarus* 54, 466-489.
71. Stixrude, L., 1997. Structure and sharpness of phase transitions and mantle discontinuities. *J. Geophys. Res.*, 102, 14835-14852.
72. Tackley, P.J., 2002. Strong heterogeneity caused by deep mantle layering. *Geochem. Geophys. Geosyst.*, 3(4), 10.1029/2001 GC000167.
73. Taylor, S.R., McLennan, S.M., 1985. *The Continental Crust: Its Composition and Evolution*. Blackwell, Oxford.
74. Taylor, R.S., McLennan, S.M., 1995. The geochemical evolution of the continental crust. *Rev. Geophys.*, 33, 241-265.
75. Thomsen, L., 1970. On the fourth-order anharmonic equation of state of solids. *J. Phys. Chem. Solids*, 31, 2003-2016
76. Ullmann, W., Pankov, V.L., 1976. A new structure of the equation of the state and its application in high-pressure physics and geophysics. *Veröff. Zentralinst. Physik der Erde*, 41, 1-201.
77. Van den Berg, A.P., Yuen, D.A., 1998. Modelling planetary dynamics by using the temperature at the core-mantle boundary as a control variable: effects of rheological layering on mantle heat transport. *Phys. Earth Planet. Int.*, 108, 219-234.
78. Van Keken, P.E., Yuen, D.A., 1995. Dynamical influences of high viscosity in the lower mantle induced by the steep melting curve of perovskite: effects of curvature and time dependence. *J. Geophys. Res.*, 100, No. B8, 15233-15248.
79. Van Keken, P.E., Ballentine, C.J., 1999. Dynamical models of mantle volatile evolution and the role of phase transitions and temperature-dependent rheology. *J. Geophys. Res.*, 104, 7137-7151
80. Vashchenko, V.Y., Zubarev, V.N., 1963. Concerning the Grüneisen constant. *Soviet Phys.-Solid State (Engl. translation)*, 5, 653-655.
81. Walzer, U., Hendel, R., 1997a. Time-dependent thermal convection, mantle differentiation and continental-crust growth. *Geophys. J. Int.*, 130, 303-325.
82. Walzer, U. and Hendel, R., 1997b. Tectonic episodicity and convective feed-back mechanisms. *Phys. Earth Planet. Interiors*, 100, 167-188.
83. Walzer, U. and Hendel, R., 1999. A new convection-fractionation model for the evolution of the principal geochemical reservoirs of the Earth's mantle. *Phys. Earth Planet. Interiors*, 112, 211-256.
84. Walzer, U., Hendel, R., Baumgardner, J., 2003a. Variation of non-dimensional numbers and a thermal evolution model of the Earth's mantle. In: Krause, E., Jäger, W.(Eds.), *High Performance Computing in Science and Engineering '02*. Springer-Verlag, Berlin Heidelberg New York. pp. 89-103. ISBN 3-540-43860-2.

85. Walzer, U., Hendel, R., Baumgardner, J., 2003b. Viscosity stratification and a 3-D compressible spherical shell model of mantle evolution. In: Krause, E., Jäger, W., Resch, M., (Eds.), High Performance Computing in Science and Engineering '03. Springer-Verlag, Berlin Heidelberg New York. pp. 27-67. ISBN 3-540-40850-9.
86. Walzer, U., Hendel, R., Baumgardner, J., 2003c. Generation of plate-tectonic behavior and a new viscosity profile of the Earth's mantle. In: Wolf, D., Münster, G., Kremer, M. (Eds.), NIC Symposium 2004. NIC Series 20, pp. 419-428. ISBN 3-00-012372-5.
87. Walzer, U., Hendel, R., Baumgardner, J., 2004. The effects of a variation of the radial viscosity profile on mantle evolution. *Tectonophysics*, 36 pp., accepted for publication.
88. Walzer, U., Ullmann, W., Pankov, V.L., 1979. Comparison of some equation-of-state theories by using experimental high-compression data. *Phys. Earth Planet. Interiors*, 18, 1-12.
89. Weidner, D.J., 1986. Mantle models based on measured physical properties of minerals. In: Saxena, S.K. (Ed.), *Chemistry and Physics of Terrestrial Planets*. Springer, Berlin. pp. 251-274.
90. Weidner, D.J., Chen, J., Xu, Y., Wu, Y., Vaughan, M.T., Li, L., 2001. Subduction zone rheology. *Phys. Earth. Planet. Int.* 127, 67-81.
91. Wetherill, G.W., 1986. Accumulation of the terrestrial planets and implications concerning lunar origin. In: Hartmann, W.K., Philips, R.J., Taylor, G.J. (Eds.), *Origin of the Moon*. Lunar and Planetary Institute, Houston. pp. 519-550.
92. Woodhead, J.D., McCulloch, M.T., 1989. Ancient seafloor signals in the Pitcairn Island lavas and evidence for large amplitude, small length scale mantle heterogeneities. *Earth Planet. Sci. Lett.*, 94, 257-273
93. Xie, S., Tackley, P.J., 2003. Evolution of helium and argon isotopes in a convecting mantle. *Phys. Earth Planet. Int.*, submitted.
94. Yale, L.B., Carpenter, S.J., 1998. Large igneous provinces and giant dike swarms: proxies for supercontinent cyclicity and mantle convection. *Earth Planet. Sci. Lett.*, 163, 109-122.
95. Yang, W.-S., 1997. Variable viscosity thermal convection at infinite Prandtl number in a thick spherical shell. Thesis, Univ. of Illinois, Urbana-Champaign.
96. Yuen, D.A., Cserepes, L., Schroeder, B.A., 1998. Mesoscale structure in the transition zone: dynamical consequences of boundary layer activities. *Earth Planets Space*, 50, 1035-1045.
97. Zerr, A., Boehler, R., 1993. Melting of (Mg,Fe)SiO₃-perovskite to 625 kilobars: indication of a high melting temperature in the lower mantle. *Science*, 262, 553-555.
98. Zerr, A., Boehler, R., 1994. Constraints on the melting temperature of the lower mantle from high-pressure experiments on MgO and magnesio-wüstite. *Nature*, 371, 506-508.